



Headcut advance modeling in stratified soils  
by Dean Allen La Tray

A thesis submitted in partial fulfillment of the requirements for the degree of Master of Science in  
Environmental Engineering  
Montana State University  
© Copyright by Dean Allen La Tray (1996)

Abstract:

Headcuts, defined as a natural vertical drop in the bed elevation of an erosive channel, are a significant mechanism of soil erosion. Impinging flow at the overfall concentrates flow energy in a localized area. Headcut development is a transient event, with progressive erosion causing expansion of the scour zone and a concurrent upstream migration of the headcut position. Much past research has focused on modeling headcut formation and movement, but no existing model has been generally tested and accepted. The erosive process is complex, highly variable, and not well understood. A headcut model could be applied to predict earthen spillway damage and to other cases where catastrophic localized scour is of concern.

The current study is designed as a theoretical and experimental investigation of headcut erosion in stratified soils. A two-dimensional, analytic model is constructed and predicts headcut advance rate for the case of a cohesive soil layer overlying a non-cohesive soil base. The model integrates two primary processes: scour hole formation in the base soil and mass failure of the cohesive surface layer. A laboratory-scale physical model is used to test and calibrate the analytical model under ideal, controlled conditions.

Soil mass failure is modeled as a cantilevered beam failing in bending, with soil tensile strength as the limiting parameter for beam stability. Data from beam failure experiments shows decreasing tensile strength with increasing moisture content for the clay used in physical modeling. A modified cantilever model incorporates hydraulic forces acting at the headcut and predicts mass failure length of the surface layer. Applied to flume experiments, the modified analytical model predicted failure lengths with an average error of 25%. This result suggests that the cantilever model successfully represents mass failure in the two-layer soil geometry.

The integrated analytical advance model predicts linear headcut movement with time in a cyclic, self propagating mode. Flume data collected with varying discharge rates and cohesive layer thicknesses show linear headcut movement, supporting the model premise. The analytical model predicted observed rates with an average error of 40% over six data sets. The model development represents a step forward in deterministic headcut characterization and sets a precedent for headcut advance rate predictability in a dual layer geometry, which had not been specifically considered to date.

HEADCUT ADVANCE MODELING  
IN STRATIFIED SOILS

by

Dean Allen LaTray

A thesis submitted in partial fulfillment  
of the requirements for the degree

of

Master of Science

in

Environmental Engineering

MONTANA STATE UNIVERSITY-BOZEMAN  
Bozeman, Montana

July, 1996

© COPYRIGHT

by

Dean Allen LaTray

1996

All Rights Reserved

N378  
L352

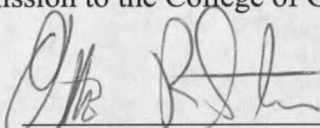
APPROVAL

of a thesis submitted by

Dean Allen LaTray

This thesis has been read by each member of the thesis committee and has been found to be satisfactory regarding content, English usage, format, citations, bibliographic style, and consistency, and is ready for submission to the College of Graduate Studies.

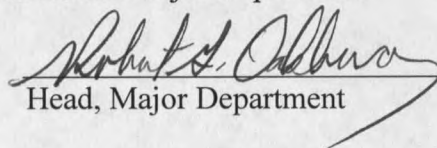
Dr. O. R. Stein

  
\_\_\_\_\_  
Chairperson, Graduate Committee

17 July 1996  
Date

Approval for the Major Department

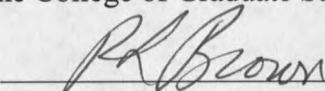
Dr. R. G. Oakberg

  
\_\_\_\_\_  
Head, Major Department

July 19, 1996  
Date

Approval for the College of Graduate Studies

Dr. R. L. Brown


  
\_\_\_\_\_  
Graduate Dean

7/30/96  
Date

## STATEMENT OF PERMISSION TO USE

In presenting this thesis in partial fulfillment of the requirements for a master's degree at Montana State University-Bozeman, I agree that the Library shall make it available to borrowers under rules of the Library.

If I have indicated my intention to copyright this thesis by including a copyright notice page, copying is allowable only for scholarly purposes, consistent with "fair use" as prescribed in the U. S. Copyright Law. Requests for permission for extended quotation from or reproduction of this thesis in whole or in parts may be granted only by the copyright holder.

  
\_\_\_\_\_  
Dean A. LaTray

\_\_\_\_\_  
Date

19 July 1996

## TABLE OF CONTENTS

	Page
1. INTRODUCTION .....	1
2. LITERATURE REVIEW .....	5
2.1 Holland and Pickup .....	5
2.2 Begin, Meyer, and Schumm .....	6
2.3 Robinson and Hanson .....	8
2.4 Temple and Moore .....	10
2.5 Stein .....	13
2.5.1 Sediment Detachment .....	14
2.5.2 Upstream and Overfall Flow .....	17
2.5.3 Plunge Pool Hydraulics .....	19
2.5.4 Equilibrium Scour Depth .....	23
2.5.5 Scour Rate .....	25
2.6 Thorne .....	27
2.6.1 Culmann Failure .....	27
2.6.2 Cantilever Beam Failure .....	29
2.7 Ajaz and Parry .....	32
3. ANALYTICAL DEVELOPMENT .....	36
3.1 Conceptual Model .....	37
3.2 Scour Model .....	38
3.2.1 Equilibrium Scour Depth .....	38
3.2.2 Scour Rate .....	38
3.2.3 Scour Width/Depth Relation .....	41
3.2.4 Final Scour Depth .....	42
3.2.5 Initial Scour Depth .....	45
3.3 Cantilever Beam Failure .....	47
3.3.1 Unmodified Beam Model .....	47
3.3.2 Mass Failure of Cohesive Surface Soil .....	50
3.3.3 Dimensionless Cantilever Model .....	53
3.4 Integrated Advance Rate Model .....	56

TABLE OF CONTENTS--Continued

4. MATERIALS AND METHODS .....	57
4.1 The Flume .....	58
4.2 Sand and Clay Materials .....	61
4.3 Fixed Overfall Experiments .....	62
4.4 Retreating Headcut Experiments .....	64
4.5 Cantilevered Beam Failure .....	67
5. RESULTS AND DISCUSSION .....	70
5.1 Physical Modeling .....	70
5.1.1 Fixed Overfall Experiments .....	70
5.1.2 Retreating Headcut Experiments .....	71
5.2 Base Layer Scour .....	72
5.2.1 Calibration of Equilibrium Scour Depth Equation .....	72
5.2.2 Scour Rate Model Calibration .....	74
5.2.3 Jet Trajectory .....	76
5.2.4 Calibration of Trajectory Refraction Coefficient .....	80
5.2.5 Final Scour Depth .....	82
5.2.6 Scour Hole Shape .....	83
5.2.7 Calibration of Scour Hole Shape Coefficient .....	83
5.2.8 Downstream Sediment Transport .....	88
5.3 Cantilever Mass Failure .....	89
5.3.1 Tensile Strength Measurement .....	89
5.3.2 Headcut Mass Failure .....	92
5.4 Integrated Advance Rate Model .....	95
6. CONCLUSIONS AND RECOMMENDATIONS .....	100
6.1 Research Conclusions .....	100
6.2 Research Summary .....	101
6.3 Recommendations for Further Study .....	104
BIBLIOGRAPHY .....	106
LIST OF SYMBOLS .....	110

## LIST OF TABLES

Table	Page
5.1. Fixed Overfall Experimental Parameters . . . . .	71
5.2. Retreating Headcut Experimental Parameters . . . . .	72
5.3. Equilibrium Scour Depth for Fixed Overfall Runs . . . . .	73
5.4. Scour Model Parameters for Fixed Overfall Runs . . . . .	75
5.5. Modeled and Observed Maximum Scour Depth . . . . .	82
5.6. Failure Period and Initial Scour Depth . . . . .	86
5.7. Observed Cantilevered Beam Failure Parameters . . . . .	90
5.8. Retreating Headcut Mass Failure Length . . . . .	93
5.9. Modeled and Observed Headcut Advance Rates . . . . .	97

## LIST OF FIGURES

Figure	Page
2.1. Initial Headcut Hydraulics. From Stein and Julien (1993). . . . .	14
2.2. Plunge Pool Definition. From Stein and Julien (1994). . . . .	21
2.3. Culmann Failure Geometry. Adapted from Thorne (1978). . . . .	28
2.4. Cantilevered Beam Stability Diagram. Adapted from Thorne (1978). . . . .	29
2.5. Stress Distribution Over Beam Depth. From Ajaz and Parry (1975). . . . .	34
3.1. Headcut Advance Cycle. . . . .	39
3.2. Scour Hole Width/Depth Relation. . . . .	41
3.3 Scour Hole Geometry with Linear Jet Trajectory. . . . .	43
3.4. Scour Hole Geometry with Modified Jet Trajectory. . . . .	45
3.5. Cantilevered Beam Model. . . . .	47
3.6. Modified Cantilevered Beam Model. . . . .	51
3.7. Mass Failure Length Sensitivity to Neutral Axis Position. . . . .	54
3.8. Mass Failure Length Sensitivity to Soil Tensile Strength. . . . .	54
3.9. Mass Failure Length Sensitivity to Flow Depth. . . . .	55
4.1. Flume Longitudinal Cross-Section (not to scale). . . . .	59
4.2. Ottawa sand particle size distribution. . . . .	61
4.3. Profile View of Cantilevered Beam Experiment. . . . .	69

LIST OF FIGURES--Continued

5.1. Scour Depth With Time for Fixed Overfall Runs. ....	76
5.2. Run SH1 Submerged Jet Trajectories. ....	78
5.3. Run SH2 Submerged Jet Trajectories. ....	78
5.4. Run SH3 Submerged Jet Trajectories. ....	79
5.5. Run SH4 Submerged Jet Trajectories. ....	79
5.6. Regression of Trajectory Refraction Coefficient. ....	81
5.7. Scour Hole Width/Depth Relation. ....	84
5.8. Regression of Scour Hole Shape Coefficient. ....	85
5.9. Soil Tensile Strength as a Function of Moisture Content. ....	92
5.10. Run CL8 Failure Length Histogram. ....	94
5.11. Modeled and Observed Mass Failure Lengths. ....	94
5.12. Observed Headcut Advance. ....	96
5.13. Observed and Modeled Headcut Advance Rates. ....	97

## ABSTRACT

Headcuts, defined as a natural vertical drop in the bed elevation of an erosive channel, are a significant mechanism of soil erosion. Impinging flow at the overfall concentrates flow energy in a localized area. Headcut development is a transient event, with progressive erosion causing expansion of the scour zone and a concurrent upstream migration of the headcut position. Much past research has focused on modeling headcut formation and movement, but no existing model has been generally tested and accepted. The erosive process is complex, highly variable, and not well understood. A headcut model could be applied to predict earthen spillway damage and to other cases where catastrophic localized scour is of concern.

The current study is designed as a theoretical and experimental investigation of headcut erosion in stratified soils. A two-dimensional, analytic model is constructed and predicts headcut advance rate for the case of a cohesive soil layer overlying a non-cohesive soil base. The model integrates two primary processes: scour hole formation in the base soil and mass failure of the cohesive surface layer. A laboratory-scale physical model is used to test and calibrate the analytical model under ideal, controlled conditions.

Soil mass failure is modeled as a cantilevered beam failing in bending, with soil tensile strength as the limiting parameter for beam stability. Data from beam failure experiments shows decreasing tensile strength with increasing moisture content for the clay used in physical modeling. A modified cantilever model incorporates hydraulic forces acting at the headcut and predicts mass failure length of the surface layer. Applied to flume experiments, the modified analytical model predicted failure lengths with an average error of 25%. This result suggests that the cantilever model successfully represents mass failure in the two-layer soil geometry.

The integrated analytical advance model predicts linear headcut movement with time in a cyclic, self propagating mode. Flume data collected with varying discharge rates and cohesive layer thicknesses show linear headcut movement, supporting the model premise. The analytical model predicted observed rates with an average error of 40% over six data sets. The model development represents a step forward in deterministic headcut characterization and sets a precedent for headcut advance rate predictability in a dual layer geometry, which had not been specifically considered to date.

## CHAPTER ONE

### 1. INTRODUCTION

A headcut, sometimes called a knickpoint, can be defined as a natural, nearly vertical drop in the elevation of a channel bed with erosive boundaries. The drop is a result of concentration of flow energy over a localized area, causing accelerated erosion. In many studied cases, the geometry creating local scour is spatially and temporally constant, such as a bridge pier or cantilevered pipe. In those cases the erosion rate can be quantified in relation to the fixed geometry. However, other instances including gully erosion and breaches of earthen spillways present conditions where erosion is transitory in space and time. Under certain conditions, progressive erosion causes deepening and widening of the scour zone and a concurrent upstream migration of the headcut position. Conditions conducive to transient localized scour can develop quite rapidly, often within a single storm event, and once developed are often self-propagating in that there is a positive feedback between the erosion and the geometry causing the erosion. The scale of this action depends on soil and hydraulic conditions, and can range from millimeters to meters. The mechanism of headcut formation and movement vary greatly.

Headcut erosion models have potential applications in several disciplines. Several headcut researchers have focused on earthen spillway damage, where in extreme cases catastrophic failure could occur. The breaching of clay caps protecting hazardous material,

due to erosion by concentrated channel flow, is another concern. A clay cap breach can cause exposure of protected waste materials and subsequent contamination at down-gradient locations. Other applications include soil erosion prediction and control and geomorphic studies of landscape evolution.

Many research efforts have been made to characterize headcut erosion. Different dominant modes of propagation have been identified in cohesive and noncohesive soils. A large amount of field and physical model data has been collected over the years under various conditions. Several models for headcut movement have been proposed, both empirical and analytical. State-of-the-art erosion models including the Revised Universal Soil Loss Equation (RUSLE) and Water Erosion Prediction Project (WEPP) are not designed to predict soil loss from localized catastrophic scour events. Different models have been used to predict the rate and distance of headcut advance on earthen spillways, but long term validation remains to be done. Due to the complexity of the erosion process and the variability of conditions, none of these models have been generally evaluated and accepted. In general, few studies have attempted to reduce models to component processes and develop them analytically.

The current study is designed as a theoretical and experimental investigation of headcut advance in stratified soils. An existing headcut is presumed; conditions for initiation are not considered. A laboratory-scale physical model was used to create ideal conditions in which critical soil and hydraulic parameters could be controlled. Concurrently, an analytical model was constructed to predict the rate of headcut propagation. The overall goal is to establish a mathematical description of headcut erosion for the specific, well defined

case of a layered soil geometry. This approach was taken to develop a solid analytical framework based on physical data which can then be used as a foundation for further model improvement.

Several specific objectives are currently addressed. First, it was desired to formulate a mathematical model to predict the rate of upstream headcut movement for the case of an erosion resistant, cohesive soil layer overlying a noncohesive soil base. Initial development was to be in two dimensions: longitudinal and vertical. The analytical model would then be tested using a physical model. An essential element of the modeling process is to determine the effects of differing hydraulic and channel bed material properties.

Given the stratified soil geometry, it was necessary to determine the role of soil mass failure as an erosion mechanism. Several researchers have observed mass failure phenomenon, but attempts at analytical quantification have been very limited. It was proposed that a cohesive layer undercut by downstream erosion would fail in bending as a cantilevered slab. Testing the validity of this failure geometry was a fundamental part of model development.

During the course of the study it was found that cohesive tensile strength was a limiting parameter for soil stability. Because tensile strength is not widely documented, a series of experiments was planned to measure the parameter under a geometry very similar to that of the headcut. Experiments were conducted over a range of bulk density and moisture content values.

The body of this thesis is organized as follows. Chapter 2 describes existing headcut models and reviews literature directly relevant to the present study. Chapter 3 details

analytical development of the stratified soil headcut advance model. Different sections describe scour hole formation in noncohesive sand and cantilevered mass failure of the cohesive surface layer. These processes are then integrated to form the final advance model. Chapter 4 details the materials and methods used for physical modeling. Chapter 5 compares the results of the analytical and physical models and discusses model calibration. The final chapter presents conclusions and recommendations for further study.

## CHAPTER TWO

### 2. LITERATURE REVIEW

This review includes first a summary of several research efforts to model headcut movement, beginning with Holland and Pickup in 1976 and concluding with Temple and Moore in 1994. Various approaches have been taken to quantify hydraulic erosive attack and soil and rock resistance to that attack. The large majority of the studies have not broken the erosion process into component elements, but take a broader approach. Often only qualitative observations are provided, based on field or laboratory data. The missing element seems to be research that focuses analytically on specific erosion elements and coordinates the theory with physical data under controlled conditions. This is not to say that the existing models are without merit; in some cases data has been collected for years and much progress has been made in defining the modeling problem.

Secondly, the literature review gives a detailed summary of several research efforts which were used directly in conceptual development of the current headcut model. These studies address jet scour in noncohesive soil and subjects relevant to soil mass failure.

#### 2.1 Holland and Pickup

Holland and Pickup (1976) perform a flume study of knickpoint development in stratified sediment. The study observes headcut formation and movement in three

dimensions. Initial soil geometry consisted of two thin unconsolidated sand layers placed between thicker cohesive layers made of sand and plaster mix. Conclusions include informative qualitative observations on the form and process of headcut movement in stratified soils.

A distinction is made between stepped and rotating headcut morphology. The authors note that stepped knickpoints tend to maintain a vertical face as they move upstream and are characterized by a plunge pool. Stepped headcuts developed as a result of undercutting in the underlying sand layers. When the knickpoints had developed, a channel-in-channel system resulted. In plan view the headcut edge, or lip, tended to be semicircular, and retreat usually occurred when this arcuate form was breached. It was determined that headcut retreat rates generally varied positively in response to changes in discharge. The presence of sand layers stabilized, and generally lowered, erosion rates compared to tests in homogeneous cohesive material. The difference in rates was in some cases more than an order of magnitude.

Holland and Pickup reach a conclusion that sets a precedent for the current research: "...the implications of the present study are that stepped knickpoints developed on knickpoint forming horizons in stratified sediment tend to maintain their form, indicating the presence of an equilibrium condition."

## 2.2 Begin, Meyer, and Schumm

Begin et al. (1980) develop one of the first analytical models predicting headcut advance rate. Different model forms are presented for rotating and stepped headcut

geometries. Conservation of eroded sediment mass and calculation of downstream sediment transport rate provide a basis for the mathematical development.

The study examines degradation of channels in response to baselevel lowering, accomplished by a discrete drop in flume outlet elevation at time zero during physical data collection. A fundamental tenant of the model combines a sediment continuity equation and a sediment discharge relation to predict channel slope as a function of time and distance from the flow outlet. The differential equation generated is a version of the heat (diffusion) equation, and the solution predicts a decrease in channel slope with both time and distance from the outlet. Sediment discharge is assumed proportional to bed slope, and therefore also decreases accordingly. The authors point out that any chosen sediment discharge relation could be introduced to the model, which could change the channel slope solution.

The geometry used for stepped headcut migration is simple parallel retreat of a vertical headcut face. A sediment mass continuity analysis yields an expression for headcut advance rate:

$$dx/dt = \frac{q_{sd}}{\gamma_s D_h} \quad (2.1)$$

where:  $dx/dt$  = headcut advance rate

$q_{sd}(x,t)$  = downstream sediment discharge rate per unit width

$\gamma_s$  = bulk sediment weight per unit volume

$D_h$  = headcut height (assumed constant)

The final form of this relation involves substitution for the sediment discharge rate, predicted

to decrease as described earlier. Thus the advance rate decreases proportionally. The authors state that "it becomes increasingly difficult for the channel to cope with the amount of sediments produced in the plunge pool. The expected result is an increased dependence of the velocity of migration of the headcut on the transporting ability of the channel."

The authors collect flume data that indeed shows a decreasing advance rate over time, but this is significantly complicated by factors including channel armoring caused by gravel and coarse sand. The proposed model fits the data only over an initial period of each run presented.

Begin et al. (1980) conclude that the mechanism of downstream transport of sediments supplied by the receding headcut becomes very important. The diffusion model is somewhat qualified by one summary statement: "...the special case of a headcut with a plunge pool at its base represents a most efficient mechanism for disposing of sediments and inducing headcut migration, and it may result in headcut migration with a constant rate."

### 2.3 Robinson and Hanson

Over the last decade Robinson and Hanson have published several papers examining headcut erosion, focusing on applications to earthen spillways. They present one of the only headcut advance models incorporating a mass wasting component.

In research most relevant to the current work, Robinson and Hanson (1994a) propose a headcut advance model composed of a boundary stress prediction model and a mass failure model. The basic headcut geometry is very similar to that used by Stein and Julien (1993), in which a free-falling nappe is generated at a vertical headcut position. Results of work by

Robinson (1992) determining hydraulic shear stress distribution over an unerodible vertical and horizontal floor below an overfall are incorporated. Resulting sediment detachment is calculated with an excess shear stress equation. A mass failure model based on soil properties and applied forces is developed to characterize the headcut advance. The model geometry assumes shear failure along a Culmann plane passing through the headcut toe. Failure occurs due to undercut and deepening of the overfall face. The length of the failure block is assumed to be equal to half of the overfall height. The model time scale is introduced by the period estimated for erosion of the mass failure material from the scour region.

The authors acknowledge significant simplifying assumptions made in model development. There seem to be some fundamental weaknesses. A Culmann type failure is unlikely to occur in materials with appreciable cohesion, as determined by Thorne (1978). The soil surface in the jet impingement area would not be horizontal, as assumed in the stress distribution calculations. Also, the mechanism used for lag time between failure events seems to poorly represent the physical case. Robinson and Hanson recognize the need for further research and give constructive recommendations on specific points for study. Significant among these is a reliable means of estimating soil erodibility as well as the length and time scales of mass wasting.

Recent Robinson and Hanson publications (1994b, 1994c, 1994d) present results of large scale flume experiments. There is no attempt to apply a deterministic headcut erosion model, although qualitative observations are made on the effects of different physical variables. Advance rates are measured under various conditions, providing valuable data.

The basic setup of the experiments involved compacted soil placed in a large flume (29 m long) in which a pre-formed headcut was constructed. Various overfall heights, discharge rates, degrees of soil compaction and density, and moisture contents were used. Several important points are made. Headcut movement data displayed a typically linear advance with time. Advance rates varied over a large range, from 0.3 to 30 cm/min. Observed rates decreased with higher soil densities and unconfined compressive strength. Different erosion processes were noted, corresponding to the stepped and rotating modes described by other researchers.

A portion of the 1994b study examined the influence of a basal sand layer on headcut advance. The sand effect depended on characteristics of the overlying layer. For highly erodible surface layers the sand had little impact on the headcut advance rate. The overfall in that case typically retreated with a sloping, rather than vertical, face. For overlying material with greater erosion resistance, the sand layer dramatically increased the headcut movement. This finding is an interesting contrast to the earlier observations of Holland and Pickup (1976). Robinson and Hanson (1994b) note that "Classical mass wasting failures were observed as the sand was removed from the base of the overfall, tension cracks formed, and large blocks of soil were removed. The headcut would move upstream with a near vertical face."

#### 2.4 Temple and Moore

Temple and Moore (1994) present a second model for headcut advance, based on a long-term joint study conducted by the Natural Resources Conservation Service (NRCS) and

Agricultural Research Service (ARS). This model also focuses on earth spillway erosion. Headcut advance is predicted using an energy based parameter to quantify the erosive attack and a headcut erodibility index to describe erosive resistance of geologic materials.

A spillway erosion prediction model was developed in three sequential phases: 1) erosion resulting in the local failure of vegetal cover, if any, and development of an area of flow concentration, 2) downward and downstream erosion in the area of flow concentration leading to formation of a vertical or near-vertical headcut, and 3) upstream advance and associated deepening of the headcut. A summary of the third phase is given here. The authors describe this component of the model as the most complex and least understood, resulting in an advance model that is necessarily semi-empirical. Model parameters were calibrated with field data from spillways that had experienced extreme flow events.

The properties of model geologic materials are represented by a headcut erodibility index,  $K_h$ . It is a strength based parameter defined as:

$$K_h = M_s(RQD/J_n) J_s (J_r/J_a) \quad (2.2)$$

where:  $M_s$  = earth mass strength number

RQD = rock quality designation

$J_n$  = joint set number

$J_s$  = relative ground structure number

$J_r$  = joint roughness number

$J_a$  = joint alteration number

Definitions and discussion on field determination of these terms is given in the appendix to

Temple and Moore (1994). For the case where there were multiple materials in the vertical profile, the depth weighted average of the log of the index for the exposed materials was used. The index range is from 0.01 for cohesionless sand to greater than 10000 for massive, hard rock.

Erosive attack was quantified by use of an energy dissipation term:

$$\dot{E} = q \gamma_w \Delta H \quad (2.3)$$

where:  $\dot{E}$  = flow energy dissipation rate per unit width of headcut

$q$  = volumetric water discharge per unit width

$\gamma_w$  = unit weight of water

$\Delta H$  = change in elevation of the energy grade line through the headcut

A threshold value of this term,  $\dot{E}_o$ , is defined as the energy dissipation rate associated with headcut erosion causing upstream advance.

The headcut advance rate equation takes the form of an excess attack relation analogous to the excess stress equation used for sediment detachment:

$$dx/dt = C(A - A_o) \quad ; \quad (A - A_o) > 0 \quad (2.4)$$

where:  $dx/dt$  = rate of headcut advance upstream

$C$  = material dependant coefficient

$A$  = hydraulic attack

$A_o$  = material dependant threshold attack level below which advance does not occur.

A substitution of terms results in a more definitive form of the equation:

$$dx/dt = C[(q\gamma_w\Delta H)^a - \dot{E}_t^a] \quad (2.5)$$

where  $a$  is an empirical constant and all other terms have been previously defined. Both the coefficient  $C$  and threshold hydraulic term  $\dot{E}_t$  are further presented as functions of the headcut erodibility index. An optimization approach was taken to fit the model to field data by minimizing the summed differences between predicted and observed headcut advance distances. Predicted advance distances were generally consistent with observed values, although considerable data scatter was observed.

In concluding, Temple and Moore state that additional field data and analysis should improve both headcut advance prediction and procedures for determining the erodibility index. They find that data is most scarce for conditions involving high discharges and erosion resistant geologic materials.

### 2.5 Stein

In his doctoral dissertation (1990) and several later publications (Stein and Julien (1993), Stein et al. (1993), Stein and Julien (1994)), Stein examines and develops model expressions for several aspects of headcut development and migration. The current study is based in large part on the results of his work. The following review summarizes the essential concepts and equations used in this study and referenced in following chapters.

The basic geometry and flow conditions common to Stein's different publications are shown in Fig. 2.1. Steady flow of unit discharge  $q$  in two dimensions approaches a headcut

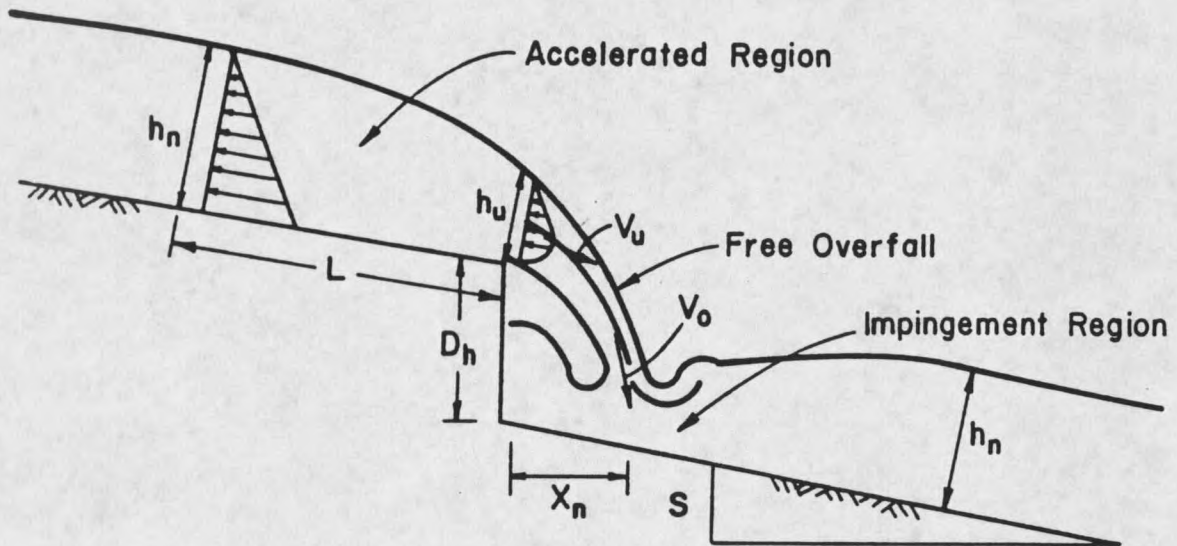


Figure 2.1. Initial Headcut Hydraulics. From Stein and Julien (1993).

over an upstream reach of constant slope. At the overfall a free-falling planar jet forms and impinges obliquely at a point below the headcut. Stein presents a physical analysis based on flow hydraulics and soil characteristics both above and below the headcut position.

### 2.5.1 Sediment Detachment

An excess shear equation is used for the rate of sediment detachment, as proposed by Foster and Meyer (1975). The sediment detachment rate can be defined as the sediment mass removed from a unit surface area per time:

$$q_s = \kappa (\tau - \tau_c)^\xi \quad (2.6)$$

where  $\kappa$  and  $\xi$  are experimentally determined constants,  $\tau$  is the applied hydraulic shear stress, and  $\tau_c$  is the critical shear stress of the bed material. The critical shear stress

represents the threshold where hydrodynamic forces are balanced by gravitational and other resisting forces of a particle on the bed surface. Sediment detachment will occur for any applied shear stress in excess of the critical value. Stein notes that although this equation has a general form, the parameters  $\kappa$ ,  $\tau_c$ , and  $\xi$  may all vary significantly under different conditions. Stein et al. (1994) give results for experiments using a fine sand ( $d_{50} = 0.15\text{mm}$ ) as follows:  $\kappa = 0.30 \text{ s}^2/\text{m}^{0.5}\text{kg}^{0.5}$ ,  $\xi = 1.5$ ,  $\tau_c = 0.35 \text{ Pa}$ . (The units of  $\kappa$  depend on the value of  $\xi$ : for  $\xi = 1.5$ ,  $\kappa = \text{s}^2/\text{m}^{0.5}\text{kg}^{0.5}$ . For  $\xi = 1.0$ ,  $\kappa = \text{s/m}$ .)

The applied hydraulic shear stress is a measure of the friction between a viscous fluid and the flow boundary. This friction is the force causing sediment detachment and creates flow resistance and energy dissipation. Both flow and boundary characteristics affect the magnitude of shear stress. Stein (1990) and Bormann and Julien (1991) translate bed shear stress to a characteristic velocity ( $V$ ) by using a friction coefficient ( $C_f$ ).

$$\tau = C_f \rho_w V^2 \quad (2.7)$$

where  $\rho_w$  = fluid mass density. For the case of impinging jet flow, the maximum shear stress in the impingement area is determined by the maximum local jet velocity, which can be substituted in the above equation. Bogardi (1974) relates the value of the friction coefficient to the relative roughness of the surface according to:

$$C_f = \frac{\theta_{cr}}{B} (d_{50}/Y_b)^x \quad (2.8)$$

where  $\theta_{cr}$  is the critical value of the Shield's number,  $B$  and  $x$  are constants,  $d_{50}$  is sediment

size, and  $Y_b$  is the diffused jet thickness. Bormann and Julien (1991) give a summary of several research efforts to quantify the parameters  $B$  and  $x$ , suggesting values of 2.0 - 2.9 for  $B$  and 0.19 - 1.20 for  $x$ . Both Stein and Bormann use a value of 2.0 for  $B$ . In developing an expression for equilibrium scour depth (described in following sections), Bormann shows that the value of the exponent  $x$  is of significant importance. The original value used by Bogardi is 0.41, but Bormann found better predictive results with  $x = 0.5$ . Bormann suggests that the exponent depends on flow geometry and bed porosity. Stein et al. (1993) successfully use Bormann's results without modification for experiments conducted in two different noncohesive sand sizes.

The critical Shield's number relates to critical shear stress according to:

$$\tau_c = \theta_{cr} (\gamma_s - \gamma_w) d_{50} \quad (2.9)$$

where  $\gamma_s$  = sediment particle specific weight and  $\gamma_w$  = water specific weight. (Note the distinction between particle specific weight and sediment bulk specific weight.)

Stein references the results of Julien and Simons (1985) in relating shear stress to a power function of Reynolds number ( $Re$ ). The form of the equation depends on the assumption made in calculating the (Darcy-Weisbach) friction factor. The Blasius equation used by Stein is applicable for turbulent flow over a hydrodynamically smooth boundary. The Manning equation applies to turbulent flow over a hydrodynamically rough boundary, and the Chezy equation covers very deep turbulent flow. The Blasius equation gives the Darcy-Weisbach friction factor ( $f$ ) as:

$$f = 0.22 / Re^{0.25} \quad (2.10)$$

which leads to the friction coefficient employed by Stein, applicable to cohesive soils:

$$C_f = (0.22/8)Re^{-0.25} \quad (2.11)$$

where  $Re = v h_n / \nu$ ,  $v$  is the average flow velocity,  $h_n$  is flow depth orthogonal to the average velocity, and  $\nu$  is the kinematic viscosity of the fluid.

The sediment detachment rate can be written in terms of sediment continuity as the product of sediment bulk density ( $B_d$ ) and the change in scour depth ( $D$ ) with time.

Combining this with Eq. 2.6 yields:

$$B_d(dD/dt) = \kappa(\tau - \tau_c)^\xi \quad (2.12)$$

### 2.5.2 Upstream and Overfall Flow

Stein (1990) makes a detailed examination of the flow acceleration through the channel reach leading to a free overfall in order to determine the shear stress distribution over that length. For the case where flow detaches from the bed at the brink, atmospheric pressure exists along the lowest streamline. Because of the reduced overfall pressure, flow velocity increases and depth decreases over a short upstream reach to the brink. It is critical to know the overfall flow depth and velocity as these parameters determine the nappe characteristics below the headcut. Stein uses an energy based equation developed by Hager (1983, 1984) to determine these values as a function of upstream flow parameters:

$$V_n/V_u = h_u/h_n = F_r^2/(F_r^2 + 0.4) \quad (2.13)$$

where  $V_n$  and  $h_n$  are upstream normal flow velocity and depth,  $V_u$  and  $h_u$  are brink velocity and depth, and  $F_r$  is the flow Froude number. It is noted that this equation is valid only for supercritical flow ( $F_r > 1.0$ ). Given the unit discharge ( $q$ ), the continuity equation relates discharge, depth, and velocity for both upstream and overfall flow:

$$q = V_n h_n = V_u h_u \quad (2.14)$$

Julien and Simons (1985) give an equation for upstream normal flow depth as a function of bed slope ( $S$ ) and flow Reynolds number:

$$h_n = a S^b Re^c \quad (2.15)$$

where the values of  $a$ ,  $b$ , and  $c$  depend on flow and boundary conditions. For turbulent flow over a smooth boundary (Blasius assumption), the coefficients are:

$$a = (0.22v^2/8g)^{1/3}$$

$$b = -1/3$$

$$c = 7/12$$

With the above equations it is possible to calculate flow parameters at the overfall for a given unit discharge and channel slope.

The upstream hydraulic shear stress can also be written as a function of flow depth and channel slope (Stein, 1990):

$$\tau_n = -\rho_w g h_n S \quad (2.16)$$

where  $\rho_w$  = fluid mass density. This basic equation does not account for the flow drawdown in the accelerated reach.

### 2.5.3 Plunge Pool Hydraulics

As flow passes the overfall, it forms a planar free falling jet which impinges on the initial downstream soil surface at a distance  $X_n$  from the headcut face. The flow accelerates through the drop height ( $D_h$ ), causing the jet thickness to decrease and velocity to increase. At the tailwater impingement point the jet has a thickness  $Y_o$ , velocity  $V_o$ , and impingement angle  $\chi$  with the horizontal. Values of jet velocity and thickness at the point of tailwater impingement can be determined from a simple free-falling nappe relationship (Stein and Julien 1994):

$$V_o = (V_u^2 + 2gD_h)^{0.5} \quad (2.17)$$

$$Y_o = q/V_o \quad (2.18)$$

where  $D_h$  is the headcut height and  $g$  is gravitational acceleration. The jet impingement angle, measured from the horizontal, is given as:

$$\chi = \tan^{-1}[(2gD_h)^{0.5}/V_u] \quad (2.19)$$

Measured horizontally from the headcut face, the impingement point  $X_n$  can be located as:

$$X_n = V_u(2D_h/g)^{0.5} \quad (2.20)$$

A plunge pool is rapidly generated in the impingement region as the jet kinetic energy is dissipated by friction at the scour surface, as shown in Fig. 2.2. At a point below the tailwater surface the initial jet entry velocity is reduced as the jet diffuses. Upon approaching the scour surface, the jet streamlines are forced to deflect by the boundary. Flow is directed laterally away from the stagnation point where the jet centerline intersects the unscoured soil surface. Stein (1990) summarizes work done by Beltaos (1972,1974), Kobus et al. (1979), Rajaratnum (1981,1982), Yuen (1984), and Bormann (1988) investigating jet diffusion and impinging jet scour. Much of this work is directed toward characterizing the velocity field resulting from jet diffusion and boundary effects as well as the resulting surface shear forces. The shear stress is generally translated to an equilibrium scour depth. The key to quantifying impinging jet scour is first to determine the characteristic shear velocity in the impingement region and second to determine the particle stability in the scour hole. Both hydraulic and sediment parameters must be considered.

For a distance below the tailwater surface, the jet velocity remains undiminished at  $V_0$ . This volume of constant velocity can be defined as the jet potential core, having a length  $J_p$  measured from the tailwater entry point along the jet centerline. This length depends only on the jet hydraulic characteristics. For lengths beyond the potential core, the jet velocity decreases. Bormann and Julien (1991) and Stein and Julien (1994) use the following equation to determine jet velocity for centerline lengths  $J > J_p$ .

$$V/V_0 = C_d(Y/J)^{0.5} \quad ; J > J_p \quad (2.21)$$

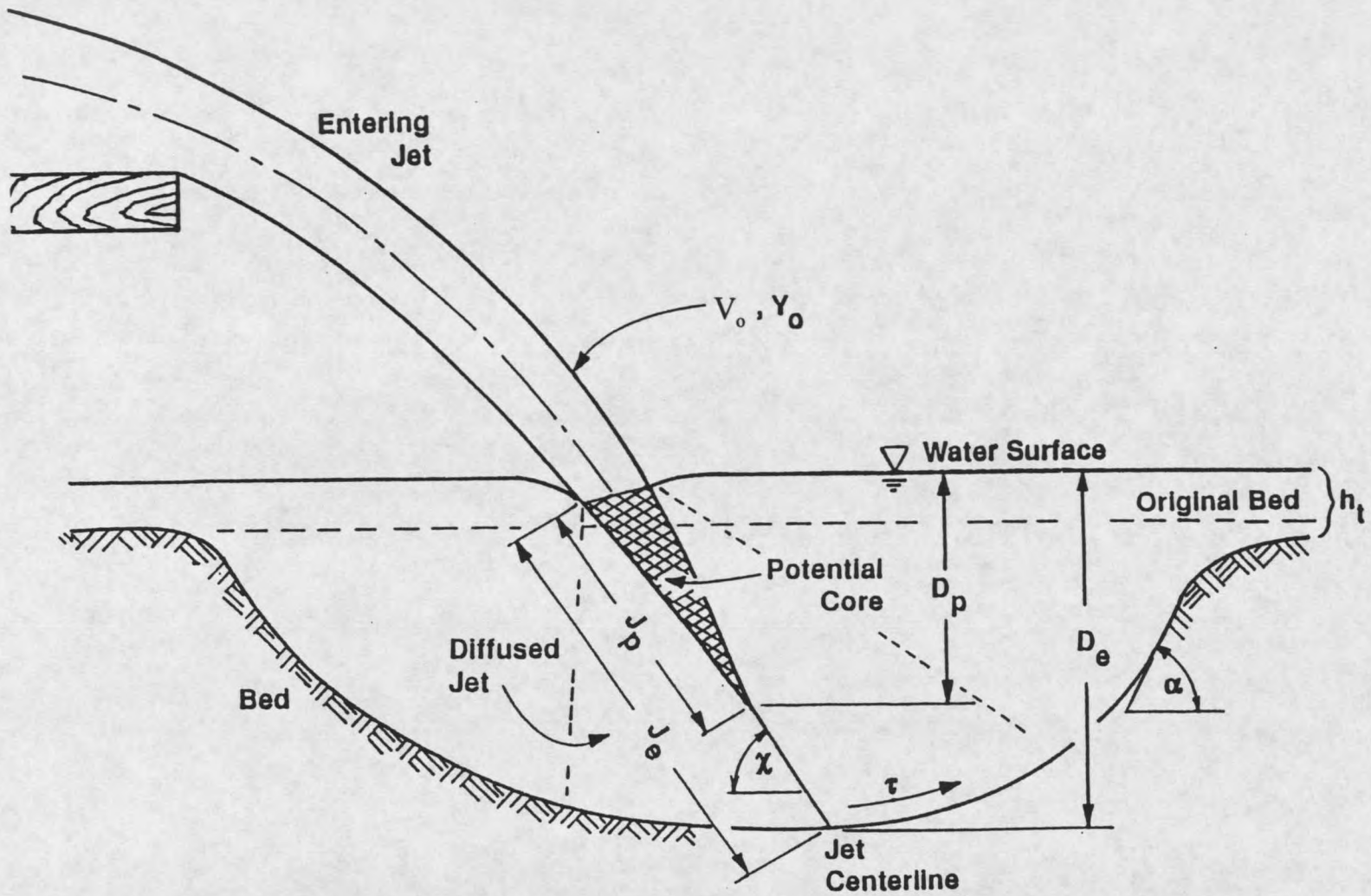


Figure 2.2. Plunge Pool Definition. From Stein and Julien (1994).

Bormann and Julien use this equation to define the velocity near the flow boundary in developing an expression for the equilibrium diffusion length ( $J_e$ ), described below.

Stein (1990) notes that there is some difficulty in determining the value of the diffusion coefficient ( $C_d$ ), which can be affected by variations in jet entry velocity, shape of the flow boundary, and the degree of boundary impermeability. Suggested values by Albertson et al. (1950), Beltaos and Rajaratnum (1973), and Yuen (1984), as reported by Bormann and Julien (1991), range from 2.0 to 2.4. Bormann (1988) uses a value of 1.8 while Stein et al. (1993) employ a higher value of 2.6, citing a well formed jet and the influencing factors above. The potential core length can be found by solving the jet diffusion equation for the case that velocity equals the impingement velocity ( $V = V_o$ ):

$$J_p = C_d^2 Y_o \quad (2.22)$$

The vertical depth of scour corresponding to the tip of the potential core can be defined as  $D_p$ :

$$D_p = C_d^2 Y_o \sin \chi \quad (2.23)$$

The scour time  $t_p$  at which this depth is reached, measured from the moment of initial surface impingement, can be derived as (Stein et al. 1993):

$$t_p = \frac{B_d D_p}{\kappa (C_f \rho_w V_o^2 - \tau_c)^{\frac{1}{2}}} \quad (2.24)$$

As long as the diffused jet exerts a shear stress in excess of the sediment critical stress, particle detachment will occur and the scour hole will grow in depth and width. Concurrently the jet diffusion length will grow and boundary velocity drops. The scour hole will reach equilibrium proportions when the applied hydraulic forces are balanced by soil particle resistance to detachment. At equilibrium the diffusion length can be defined as  $J_e$  and the scour hole depth measured from the original bed level as  $D_e$ . The values  $J_e$  and  $D_e$  are not equal because  $J_e$  is measured along the non-vertical jet trajectory.

#### 2.5.4 Equilibrium Scour Depth

Bormann and Julien (1991) derive an equilibrium scour equation based on the concepts of jet diffusion and particle stability in scour holes downstream of grade control structures. Their development considers the results of numerous investigations over a period of 50 years. Results from the developed model are compared favorably to data collected by the authors and several other researchers over a variety of geometries including wall jets, vertical jets, free overfall jets, and submerged jets.

In developing the equilibrium model, Bormann and Julien use Eq. 2.21 to define the diffused jet velocity ( $V_b$ ) by setting the diffusion length equal to the equilibrium length ( $J = J_e$ ). The continuity equation gives the jet thickness corresponding to the diffused velocity near the soil bed:

$$Y_b = Y_o (V_o / V_b) \quad (2.25)$$

Bed shear stress and the local friction coefficient ( $C_f$ ) are given by Eqs. 2.7 and 2.8 respectively. A Shields diagram can be used to find the critical value of the Shields

number in Eq. 2.8. Bormann and Julien translate the critical Shields number to critical shear stress according to Eq. 2.9.

As reported by Bormann and Julien (1991), a study of forces and moments on individual particles by Stevens and Simons (1971) examines particle stability on a sloping bed. The result is an expression for the critical shear stress required to move sediment particles up on embankment angle  $\alpha$  in the direction of flow. The expression is given as a ratio of the shear stress on a sloping bed ( $\tau_b$ ) to that for a flat bed ( $\tau_{cr}$ ).

$$\tau_b / \tau_{cr} = \sin(\phi + \alpha) / \sin\phi \quad (2.26)$$

where  $\phi$  = the sediment angle of repose.

Bormann and Julien derive the following expression for the equilibrium diffusion length  $J_e$ .

$$J_e = \left[ \frac{\rho_w \sin\phi}{B(\gamma_s - \gamma_w) \sin(\phi + \alpha)} \right]^{2/(2+x)} \frac{C_d^2 V_o^{4/(2+x)} Y_o^{(2-x)/(2+x)}}{d_{50}^{(2-2x)/(2+x)}} \quad (2.27)$$

where  $x$  is the constant in Eq. 2.8 and all parameters are as previously defined. Bormann and Julien use  $x = 0.5$  in their study. Substitution yields the final form of the equation.

$$J_e = \left[ \frac{\gamma_w \sin\phi}{B g (\gamma_s - \gamma_w) \sin(\phi + \alpha)} \right]^{0.8} \frac{C_d^2 V_o^{1.6} Y_o^{0.6}}{d_{50}^{0.4}} \quad (2.28)$$

It is noted that a choice of varying values for the parameter set  $\alpha$ ,  $C_d$ , and  $B$  can result in identical values of  $J_e$ .

Bormann and Julien reference a study by Yuen (1984) in assuming that the jet follows a linear trajectory following tailwater entry. For a free jet, this makes the angle of jet intersection with the scour boundary equal to the angle of tailwater entry. This assumption allows calculation of the equilibrium scour depth ( $D_e$ ) measured from the original bed level.

$$D_e = J_e \sin\chi - h_t \quad (2.29)$$

where  $\chi$  = tailwater impingement angle, and  $h_t$  = tailwater depth. Bormann and Julien point out that ideally a free jet is surrounded by atmospheric pressure as it enters the tailwater. In this case the jet trajectory is not affected by gravity, being neutrally buoyant, or by the Coanda effect. The Coanda effect would exert an influence if pressures were unequal on opposite sides of the jet, such that a vortex was formed on one side. This would be the case for a non-aerated overfall nappe.

#### 2.5.5 Scour Rate

Stein et al. (1993) presents solutions to a differential equation for the rate of vertical scour by an impinging jet. Three equations are given, depending on the value of the exponent of excess shear equation 2.6. Stein suggests an exponent value of 1.5 for non-cohesive sediments, yielding the following expression for the time-depth relation of scour beyond the potential core depth  $D_p$ :

$$T^* - T_p^* = (D^* - D_p^*)^{0.5} \left( 1 - \frac{2}{D^* - 1} \right) - 1.5 \arcsin(2D^* - 1) \Big|_{D_p^*}^{D^*} ; D^* > D_p^* \quad (2.30)$$

All time and depth terms are dimensionless, scaled to the scourhole equilibrium depth  $D_e$  and a reference time of no physical significance  $T_r$ .  $D^*$  is defined as  $D/D_e$ , and  $T^*$  as  $T/T_r$ .  $T_p^*$  is the normalized time corresponding to the depth of potential core scour ( $T_p/T_r$ ). Reference time  $T_r$  is defined as:

$$T_r = \frac{B_d D_e}{\kappa \tau_o^\xi} \left( \frac{D_e}{D_p} \right)^\xi = \frac{B_d D_e}{\kappa \tau_c^\xi} \quad (2.31)$$

Within the potential core, jet velocity and shear stress are constant at  $V_0$  and  $\tau_o$ . Shear stress can be determined by substituting  $V_0$  in Eq. 2.7. The resulting scour rate is also constant:

$$T^* = D^* \left( \frac{D_p^*}{1 - D_p^*} \right)^\xi ; \quad D^* \leq D_p^* \quad (2.32)$$

Critical shear stress  $\tau_c$  can be calculated by setting the scour rate equal to zero at equilibrium scour depth:

$$\tau_c = \tau_o (D_p/D_e) \quad (2.33)$$

Stein et al. (1993) present model calibration results for experiments with two different sand sizes.

Work by Stein as well as Bormann and Julien summarized in the preceding sections is used as a basis for scour modeling in the current study. The initial headcut geometry presently considered is the same as that used by Stein. Predictive equations for jet velocity

and diffusion as well as other relevant parameters given in this literature review are used directly in model analytical development presented in Chapter 3. Equations 2.28 and 2.29 for equilibrium scour depth and Eqs. 2.30 through 2.33 for vertical scour rate are calibrated for materials used in physical modeling as described in Chapter 5.

## 2.6 Thorne

### 2.6.1 Culmann Failure

Thorne (1978) presents an exhaustive study of river bank stability, examining traditional methods of analysis as well as introducing new concepts. This material is of interest in the headcut study because many of the geometries and soil mechanics are very similar. Specifically, Thorne's analysis of mass wasting mechanisms are directly relevant.

In a section on stability of cohesive banks, Thorne critiques the traditional Culmann failure analysis method. The method is based on the assumption of a planar failure surface passing through the toe of the slope, shown in Fig. 2.3. This geometry is a simple form of a failure mechanism which is more likely to occur with an arced failure surface. Bank failure occurs if the gravitational forces acting on the mass above the failure plane overcome the shear forces resisting movement. An equation is given for the critical bank height necessary to precipitate this type of failure. After simplifying and substituting typical values for soil density, cohesion, and friction angle, Thorne states that "Rotational slump failures will not occur on low soft clay banks even for vertical cuts." Even considering the presence of weakening tension cracks, the lowest critical bank height is calculated as 2.5 meters. Banks of lesser height should not fail in this mode. This

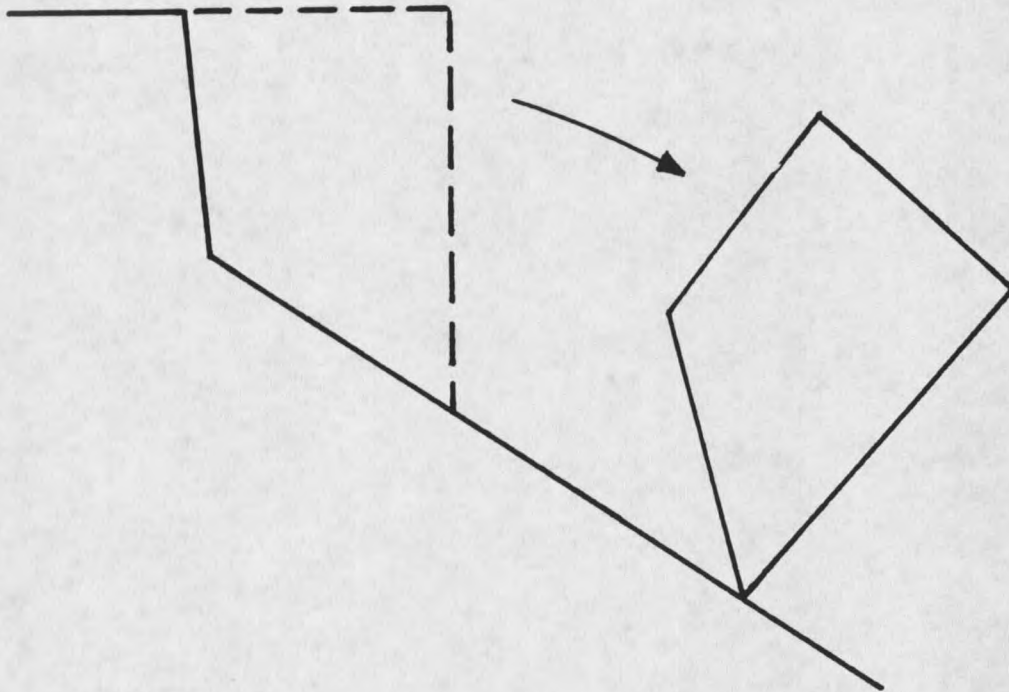


Figure 2.3. Culmann Failure Geometry. Adapted from Thorne (1978).

conclusion seems to rule out the Culmann method as an approach for headcut analysis on a small scale. The Culmann method was proposed to represent mass failure in the headcut model presented by Robinson and Hanson (1994a).

Thorne goes on to describe failure mechanisms for composite banks in which a cohesive soil layer overlies a noncohesive base. River erosion leads to lower bank retreat, leaving the overlying clay standing as a vertical cut provided that its thickness is less than the critical height for plane (Culmann) or rotational slips. If the cohesive material has sufficient strength to support its own weight, further base retreat leads to formation of a cantilever overhang. Thorne derives stability equations for three different geometries

causing failure of the overhang: shear, beam, and tension. Of these geometries, beam failure most closely represents the mass failure occurring in the present study.

### 2.6.2 Cantilever Beam Failure

In this geometry, beam failure results when the moment of the block weight about a neutral axis located on the failure plane overcomes the cohesive forces holding the block in place. Thorne's (1978) derivation treats the soil as a rigid plastic material. Above the neutral axis the soil exists in tension, and below the axis in compression. The position of the neutral axis depends on the ratio of tensile and compressive stresses at failure. An

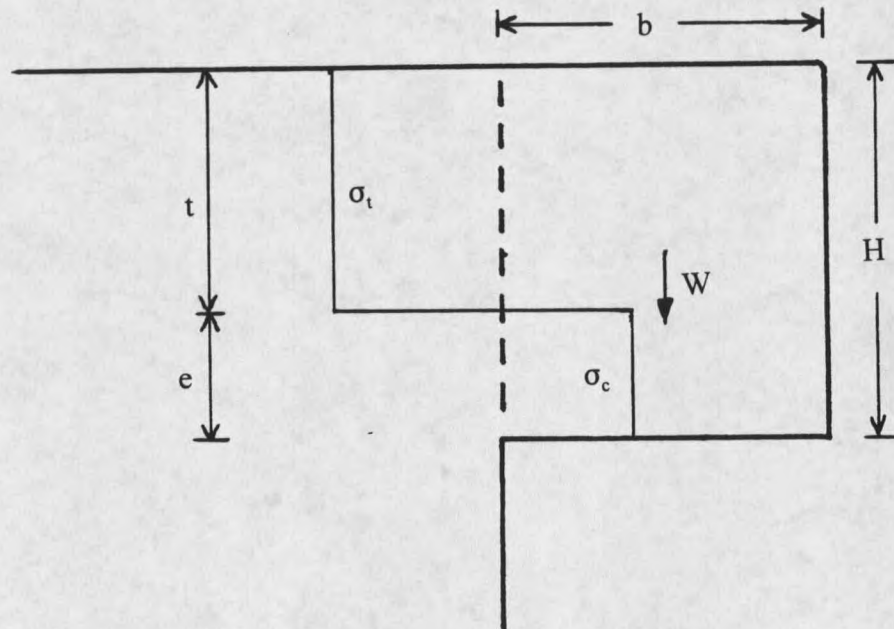


Figure 2.4. Cantilevered Beam Stability Diagram. Adapted from Thorne (1978).

adaptation of Thorne's diagram for beam failure is shown in Fig. 2.4. Due to the rigid plastic assumption, the stress distribution is constant in tension and compression over their

respective areas. This creates a stress discontinuity at the neutral axis. Rigid plastic behavior predicts no material strain prior to failure.

The stability analysis considers static forces on the beam at the point of failure. Two fundamental equations are used: one for the sum of horizontal forces acting on the failure plane, and the second for moments acting about the horizontal neutral axis.

$$\sigma_t t L = \sigma_c e L \quad (2.34)$$

$$W(b/2)L = \sigma_t t L(t/2) + \sigma_c e L(e/2) \quad (2.35)$$

where:

- $\sigma_t$  = limiting tensile stress
- $\sigma_c$  = limiting compressive stress
- $e$  = attached block depth below the neutral axis
- $t$  = attached block depth above the neutral axis
- $L$  = block width
- $b$  = block failure length
- $W$  = soil weight per unit length
- $H$  = total block depth
- $r = e/t = \sigma_T/\sigma_C$
- $\gamma_s$  = soil weight per unit volume

The fundamental equations can be solved for the block failure length ( $b$ ). Assuming no pre-existing tension or desiccation cracks, which are considered by Thorne, the failure

width can be derived as:

$$b^2 = \frac{\sigma_T H}{\gamma_s (1 + r)} \quad (2.36)$$

Thorne assumes that failure in tension and compression occur simultaneously, requiring that the tensile and compressive stresses both approach limiting values at failure. Thorne suggests a value of 0.1 for the ratio  $r$ . It is not obvious that the assumption of simultaneous tensile and compressive failure is valid. If this was the case, and taking a value of 0.1 for  $r$ , then the position of the neutral axis at failure would be very close to the base of the beam.

Thorne applies his stability analysis to field studies of river banks. The study does not attempt to predict the dimensions of failure geometry, but rather quantifies the bank stability for existing geometries. Thorne points out that existing soil pedestrian boundaries are important in controlling bank strength and failure mechanism on several scales. In many cases fissures and tension cracks determine the location of macroscale soil failure. Desiccation cracking in cohesive soils can have a significant effect on tensile strength. For surface layers the binding of vegetation roots is also a consideration. Thorne details various processes and parameters affecting soil mechanical properties, including pore water pressure, weathering, microscale structure, and others. Grissinger (1982) also presents a comprehensive summary and description of properties that influence or relate to the stability of cohesive materials.

Thorne notes the lack of available data for soil tensile failure and further comments

on attempts to predict tensile strength:

“It seems that the ratio of tensile to compressive strengths is not predictable from compression data and that the Mohr-Coulomb rupture line cannot be extrapolated back into the tension zone of the Mohr diagram. In this case data concerning the tensile strength of soil must be obtained from direct tension or beam tests.”

In his calculations, Thorne uses a working value of 4 kPa for tensile strength in alluvial silt/clay materials. As part of his study he describes construction of a simple unconfined tensile strength tester. Results of tests on field samples of cohesive bank soils range from 4 kPa to 20 kPa. Thorne consistently employs a ratio of 0.05 to 0.1 between tensile and compressive strengths. This is supported by limited data collected in more controlled laboratory experiments (Thorne et al. 1980).

The premise of cantilevered block failure described by Thorne is used as a basis for mass failure modeling described in the next chapter. Thorne's analytic development is modified considerably, however. In the current model, stress is considered to vary linearly from top to bottom in the cantilevered beam. Hydraulic forces present in the headcut geometry are added to the beam stability analysis.

### 2.7 Ajaz and Parry

Ajaz and Parry (1975) examine the stress-strain behavior of two compacted clays in tension and compression. This study is of particular value for its analysis of stress and strain distributions in clay beams under bending forces. Results of testing include direct tensile strength, flexural tensile strength (evaluated in bending), and direct compressive strength over a range of moisture contents.

Bending tests were conducted on beams 254mm long and 51mm x 51mm in cross-section, with moisture content varying from 10.4% to 15.2% for one clay and 22.2% to 31.6% for the other. The beams were supported at the ends and equal loads applied at two points equidistant from the beam midpoint. This created a central region under a constant bending moment. Strains within the beam were measured using a radiographic technique with an embedded grid of lead shot.

Observations under these conditions establish several key points. Ajaz and Parry state that:

“the specimen failed in tension as expected and not in shear, and indicated that complete failure occurred when the average tensile strain attained a critical value. The strains along the mid-length of the beam for both clays were found to vary linearly with the depth of the beam...”

Stresses were calculated using a differential method based on measured strains and applied bending moment. These calculations show a stress distribution nearly linear with the depth of the beam at times prior to failure. Figure 2.5 shows stress distributions calculated for increasing increments of applied bending moment for two different clays. However, at failure the distribution in both tension and compression zones becomes non-linear, as shown by the dashed line in Fig. 2.5. This is consistent with the stress distribution in an elastoplastic material.

Significantly, the stress calculations also show the neutral axis between areas of tension and compression lying very near the horizontal plane of symmetry. With a linear stress distribution, this makes the magnitudes of maximum compressive and tensile stresses at the beam surfaces nearly equal up to the point of failure. In contrast, Thorne (1978) suggests a value of 0.1 for the ratio of tension to compression at failure, which would place

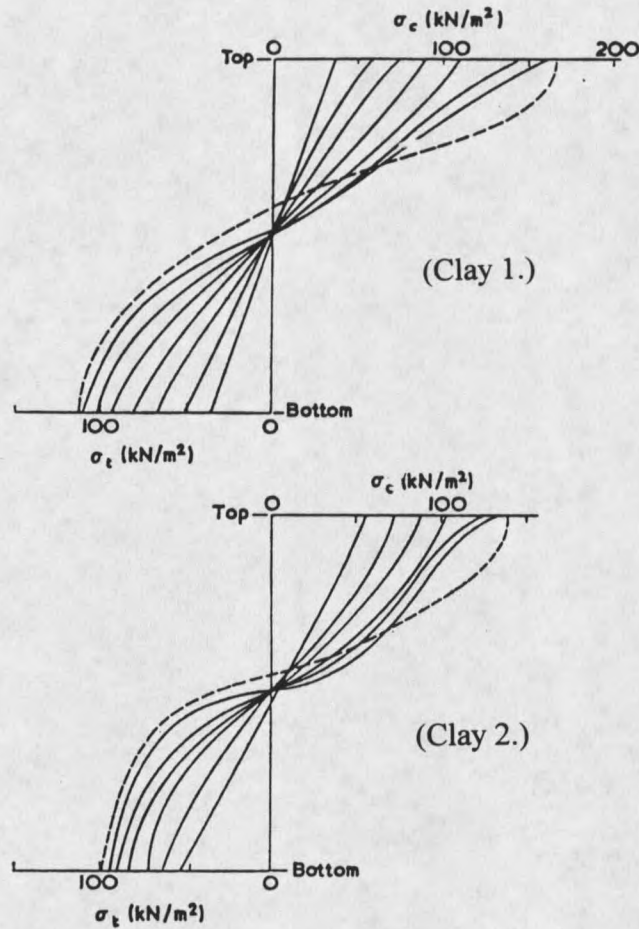


Figure 2.5. Stress Distribution Over Beam Depth. From Ajaz and Parry (1975).

the neutral axis close to the bottom of the beam in a cantilever geometry. Ajaz and Parry come to a different conclusion: "It is well known that the compressive strength of clays is usually much higher than the tensile strength and therefore in a bending test at failure the soil has a compressive stress less than the compressive strength."

Several other conclusions by Ajaz and Parry are useful. A distinction is made between tensile strength and flexural tensile strength, which is taken as the maximum tensile stress derived from the applied bending moment and measured strains. For both

clays tested, the flexural tensile strength was higher than direct tensile strength. Values of flexural tensile strength vary from approximately 40 to 160 kN/m<sup>2</sup>, decreasing with increasing moisture content. Tests also showed the direct compressive strength to be much greater than direct or flexural tensile strength at the same moisture content, as expected.

In a separate publication Ajaz and Parry (1974) describe a test procedure devised to determine the relationship between uniaxial (total) stress and the resulting tensile strains of compacted clays, as well as natural or remolded soils. They note that resistance of a soil specimen to tensile stress is due to negative pore pressures and/or interparticle bonding, depending on the condition of the sample. The paper provides only representative data, giving tensile strength of Gault clay as 60 to 80 kPa at 24.6 percent moisture content. Strain at failure was measured between 0.017 and 0.025 percent strain. Deformation moduli in tension and compression were found to be unequal.

The study by Ajaz and Parry establishes a valuable precedent for analysis of beam failure in bending. Specifically it supports the premise that stress distribution in the bending beam is linear in two dimensions. The study also concludes that tensile stress is the limiting parameter for beam stability and that the neutral stress axis lies close to the beam center. These points are incorporated into the current mass failure model developed in Chapter 3.

## CHAPTER THREE

### 3. ANALYTICAL DEVELOPMENT

This chapter develops an expression for the rate of headcut migration in a layered sediment geometry with a cohesive layer overlying a noncohesive base. The development involves two independent models which are integrated to produce the final rate equation. The first model represents the rate and geometry of scour hole formation by an impinging jet in noncohesive soil. Existing models were calibrated to predict equilibrium scour hole depth ( $D_e$ ) and the rate of maximum hole depth increase with time. The models used are based primarily on the work of Stein et al. (1993), Stein and Julien (1994), and Bormann and Julien (1991). Additionally, an analysis of the two dimensional scour hole form is presented. Together, the shape and rate of scour hole formation establish the time scale of headcut advance in the layered sediment model.

The second model represents the mass failure of the cohesive surface soil layer. During the process of scour hole formation the cohesive layer is undercut, leading to eventual failure under its own weight and external forces. The cohesive layer is modeled as a cantilevered beam in two dimensions, and an expression for the failure length of the beam is derived as a function of hydraulic and soil parameters. Thorne's (1978) model of cantilevered block failure in river banks is used as the basis for the beam model and modified to include additional forces present in the headcut geometry. The cantilevered beam failure

establishes the length scale of the headcut advance rate in the integrated model.

The above models are then combined to give an equation for the headcut advance rate. This equation predicts a linear upstream advance with time, occurring in discrete steps as each mass failure event occurs.

### 3.1 Conceptual Model

The soil geometry considered for the headcut model consists of two distinct layers: a thick, non-cohesive base layer and a thinner cohesive surface layer. Both soils are homogeneous, without any pre-existing cracks or ped boundaries. Both layers are of uniform, constant thickness. Throughout the physical data collection both soils are saturated, although the moisture content of the cohesive surface layer is varied.

The flow geometry considered is that of steady, uniform flow over an upstream reach of constant slope, represented in two dimensions, which then approaches a pre-existing overfall and forms a free falling nappe. The flow accelerates through a distance equal to the overfall height ( $D_h$ ) and impinges on the downstream soil. The overfall height is equal to or greater than the thickness of the surface soil layer. Impinging flow can be considered a jet with certain velocity and thickness. A scour hole is rapidly generated in the impingement region, as the flow shear stress is initially in excess of the critical shear stress required to remove a particle from the surface. After leaving the plunge pool, flow continues downstream and returns to the upstream flow depth.

Upstream headcut advance in this geometry occurs cyclically. Each cycle encompasses a discrete advance length and occurs over a certain time period. The advance

rate model represents a single cycle, bounded in time by successive mass failure events which are presumed to happen instantaneously. Over the cycle period, the headcut position advances upstream a distance equal to one mass failure length. Prediction of that length establishes the length scale of the advance model. The duration of the cycle period is controlled by the scour rate of the non-cohesive base layer. During the cycle, the base layer is eroded both vertically and horizontally in the upstream direction until undercut precipitates the next mass failure. Prediction of the scour rate and geometry, dependant on soil and hydraulic parameters, establishes the time scale of the model.

## 3.2 Scour Model

### 3.2.1 Equilibrium Scour Depth

At a fixed overfall position, maximum scour depth  $D_e$  will increase until an equilibrium condition is reached, at which hydraulic forces and soil particle stability are balanced. Calculation of the equilibrium depth is necessary to scale the dimensionless scour rate model developed by Stein et al. (1993). Equations 2.28 and 2.29, presented by Bormann and Julien (1991) for equilibrium scour hole depth, were used without modification for this model. However, different assumptions were made to determine values of the input parameters, as described in Chapter 5.

### 3.2.2 Scour Rate

The vertical scour rate model for non-cohesive soils developed by Stein was used as a basis for the scour model. Stein's rate equation predicts maximum scour depth as a

function of time over the range of hole formation at a fixed overfall. In the present model the overfall position changes with time, and equilibrium scour depth is never reached. Rather, the scour depth as measured from the original soil layer surface varies within a fixed interval during the failure cycle. Prediction of the scour rate over this interval is the goal of the scour portion of the model. The second form of Stein's equation, based on non-cohesive sediment transport, was calibrated as described in Chapter 5.

Figure 3.1 illustrates the range of scour depth over the model cycle. Maximum scour

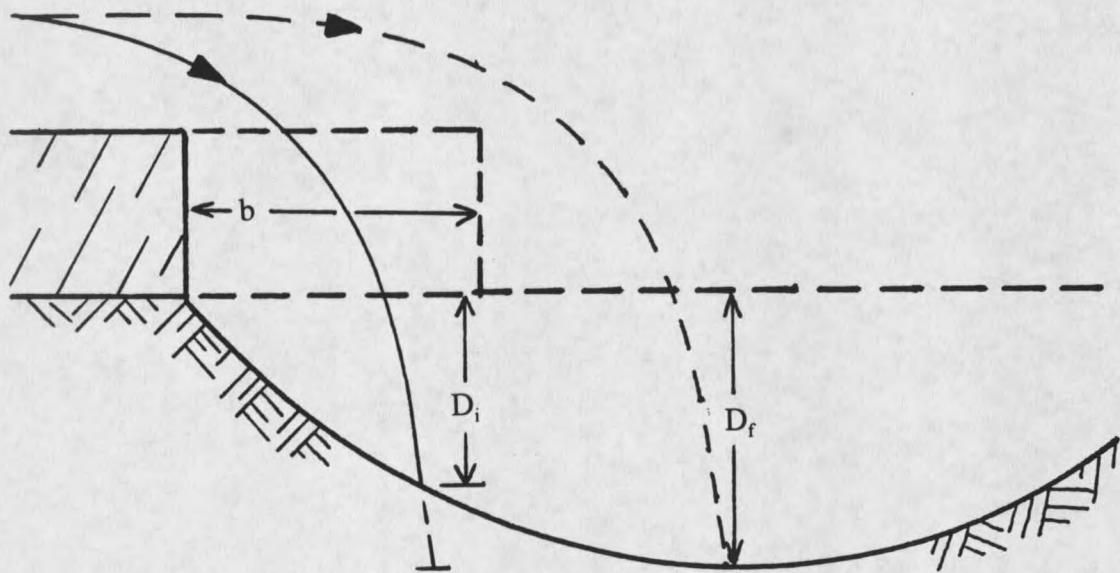


Figure 3.1. Headcut Advance Cycle.

depth  $D_f$  is reached at the end of the cycle, immediately prior to slab failure. This depth limit translates via the scour rate equation to the time  $T_f$  defining the end of the failure cycle. The lower depth limit  $D_i$  is the initial scour depth occurring at the beginning of the failure interval, immediately after slab failure. At this time, the point of maximum scour (jet

centerline) is shifted upstream by a discrete distance, impinging at a new point on the upstream limb of the existing scour hole, as shown in Fig. 3.1. The lower depth limit translates to the time defining the start of the failure cycle,  $T_i$ .

The failure cycle period is defined mathematically by the depth limits of the dimensionless scour rate Eq. 2.30:

$$T_f^* - T_i^* = (D^* - D^{*2})^{0.5} \left( 1 - \frac{2}{D^* - 1} \right) - 1.5 \arcsin(2D^* - 1) \left| \frac{D_f^*}{D_i^*} \right. \quad (3.1)$$

where  $D_f^* = D_f/D_e$ ,  $D_i^* = D_i/D_e$ ,  $T_f^* = T_f/T_r$ ,  $T_i^* = T_i/T_r$ . Reference time  $T_r$  is given by Eq. 2.31. Equation 3.1 is only valid for  $D_i^*$  greater than or equal to  $D_p^*$ , defined by Eq. 2.23. It should be noted that the scour rate equation is very sensitive to changes in the limit values. This is because small increases in scour depth take significant time over the deeper portion of the scour hole.

The challenge in modeling scour hole development then becomes accurate prediction of the initial and final scour depths necessary to calculate the cycle period. Several of the fundamental parameters can be measured directly during flume data collection: maximum scour depth ( $D_p$ ), cycle period ( $\Delta t$ ), and mass failure length ( $b$ ). It is difficult to directly measure the initial scour depth ( $D_i$ ) during data collection. However, given the cycle period and upper limit of the scour rate equation, the lower limit can be determined by iteratively solving Eq. 3.1.

### 3.2.3 Scour Width/Depth Relation

The maximum scour depth point  $D_f$  is located at the intersection of the submerged jet trajectory and the upstream scour hole limb, as shown in Fig. 3.1. Before  $D_f$  is calculated, the relationship between the endpoints of the upstream limb must be developed. At the moment of mass failure, the toe point of the scour profile (shown as point A in Fig. 3.2) is determined by the mass failure length  $b$ . It is then necessary to locate the point of

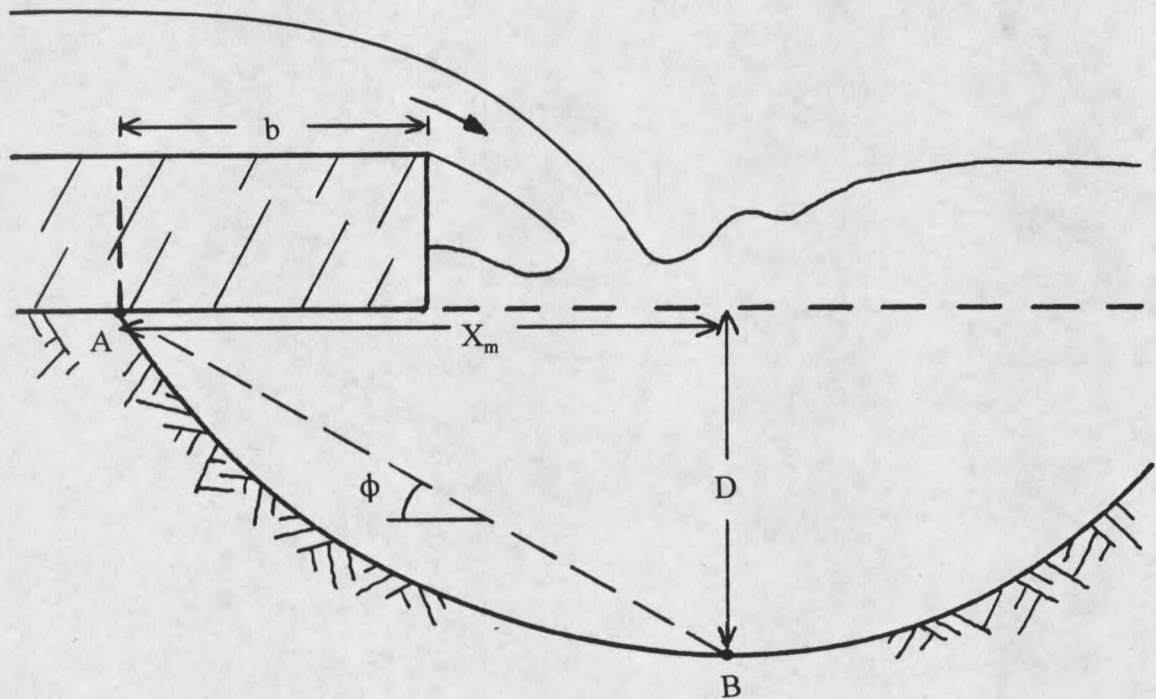


Figure 3.2. Scour Hole Width/Depth Relation.

maximum scour (shown as point B in Fig. 3.2) relative to the toe point. The relative position of points A and B is determined by analyzing scour hole half-width  $X_m$  as a function of maximum scour depth  $D$ .

Data from fixed overfall experiments, presented in Chapter 5, were used to analyze

the shape relationship. Values of scour hole half-width ( $X_m$ ) were calculated as the difference in the longitudinal position of the toe point and the maximum scour point, as shown in Fig. 3.2. The width-depth relationship was consistent over all data sets: hole width increases linearly with hole depth. The slope of the function can be well approximated by the tangent of the angle of repose:

$$D/X_m = \tan\phi \quad (3.2)$$

Linearity extends over the full range of scour hole depth. Given that the mass failure length can be predicted, and knowing the angle of repose, then the line is fixed along which the maximum scour point ( $D_f$ ) must lie at cantilevered soil failure. This line is shown dotted in Fig. 3.2.

This conclusion does not mean that the hole profile is linear, although over much of its length that may be a good assumption. Only the two endpoints of the upstream limb are related by the above equation. The shape of the intermediate profile is not represented. As intended, however, this equation allows calculation of the horizontal extent of scour as determined by scour hole depth.

#### 3.2.4 Final Scour Depth

Scour hole geometry was based on the plunge pool models used by Stein et al. (1993) and Bormann and Julien (1991). Several successive modifications to the submerged jet trajectory were made to reach a final form, with the goal of predicting the final scour depth,  $D_f$ . The first trial employed the geometry presented by previous researchers, with

the assumption that the jet continues in a linear trajectory after tailwater entry, making an angle with the horizontal equal to the angle of tailwater impingement ( $\chi$ ). This geometry is shown in Fig. 3.3. The relation characterizing the upstream scour limb presented in the

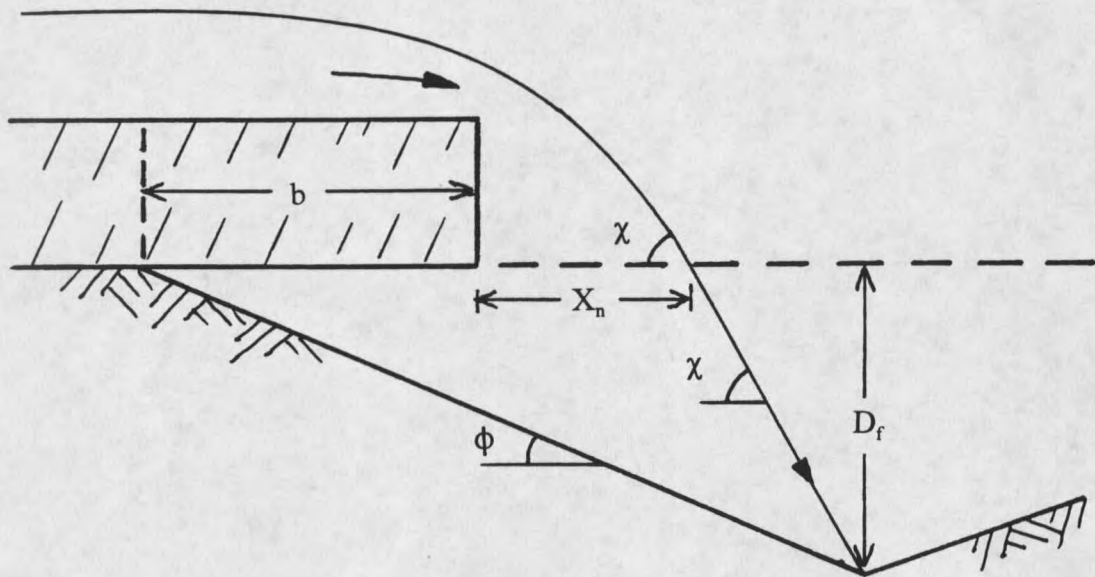


Figure 3.3 Scour Hole Geometry with Linear Jet Trajectory.

last section is incorporated. Given the values of mass failure length  $b$ , soil angle of repose  $\phi$ , and the jet impingement distance  $X_n$ , the final scour depth can be calculated according to the geometry of Fig. 3.3:

$$D_f = \frac{\tan\phi (X_n + b) \tan\chi}{\tan\chi - \tan\phi} \quad (3.3)$$

Unfortunately, application of this equation results in calculated scour depths much greater than those observed. In fact, for impingement angles less than or equal to the angle of

repose, an infinite depth is predicted.

This result suggests that the jet trajectory following tailwater entry is at an angle steeper than the impingement angle  $\chi$ . This conclusion was readily apparent during visual observation of the fixed overfall runs. Based on this idea, the maximum scour depth geometry was modified to assume a vertical jet trajectory from the tailwater impingement point. This alters the equation for  $D_f$  to the following form:

$$D_f = (X_n + b)\tan\phi \quad (3.4)$$

This correction resulted in calculated scour depths smaller than those observed in retreating headcut runs. Thus it was concluded that the actual jet trajectory is at an angle greater than the impingement angle  $\chi$ , but less than vertical.

To accommodate this conclusion, an empirical coefficient was introduced to modify the jet trajectory angle. This results in a modified form of the original scour depth equation:

$$D_f = \frac{\tan\phi (X_n + b) \tan(C_r\chi)}{\tan(C_r\chi) - \tan\phi} \quad (3.5)$$

Physically, introduction of the coefficient  $C_r$  causes downward refraction of the jet trajectory upon tailwater entry, as shown in Fig. 3.4. The term will be further referred to as the refraction coefficient. The refraction coefficient can be written as a ratio of the submerged trajectory angle to the calculated tailwater impingement angle:

$$C_r = \frac{\chi'}{\chi} \quad (3.6)$$

The coefficient was reasoned to be dependant on the impingement angle, with a greater correction necessary for small impingement angles. For the limiting case of a vertically

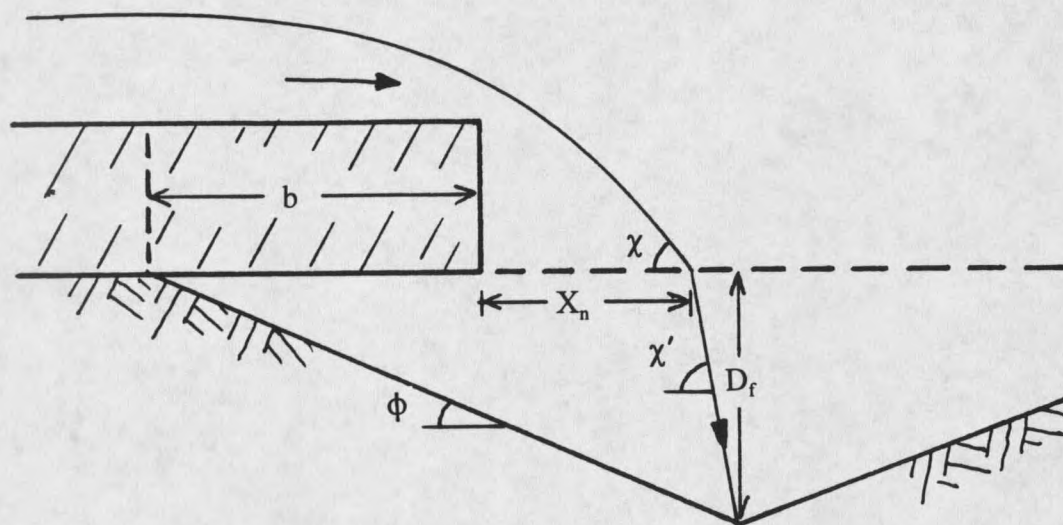


Figure 3.4. Scour Hole Geometry with Modified Jet Trajectory.

impinging jet, no trajectory modification would be necessary ( $C_r = 1.0$ ). Further development of the refraction coefficient is described in Chapter 5.

### 3.2.5 Initial Scour Depth

Given the upper limit of the scour rate equation ( $D_f$ ), the next step is to find the lower limit, or initial cycle scour depth ( $D_i$ ). At the start of the failure cycle, the jet scour point has shifted from the position of maximum scour for the previous cycle to a new point

on the upstream limb of the existing scour hole. Because the overfall position has advanced a distance equal to one mass failure length between cycles, it is reasonable that the new jet scour point also advances approximately one failure length. The initial scour depth is defined by the intersection of the jet centerline and the scour hole profile, as shown in Fig. 3.1. The position of the intersection point depends on the shape of the scour hole profile. To predict the initial scour depth, the profile shape must be quantified. Because the actual shape is unstable in the two-layer geometry, a semi-empirical shape function was introduced.

The maximum scour depth at failure locates the lowest point of the scour hole profile. Through the development of Eq. 3.5, both the vertical and longitudinal coordinates of this point are known. A second point on the profile, and the only one requiring calculation between endpoints, corresponds to the initial scour depth ( $D_i$ ). The initial scour depth then is a function of the final scour depth and the failure length. A proposed shape function is given as:

$$D_i^* = D_f^* - C_s b^* \quad (3.7)$$

where  $C_s$  = empirical constant termed the scour hole shape coefficient, and  $b^* = b/D_e$ . The function represents only the bottom portion of the hole profile, and is not intended to quantify the entire profile. It assumes profile similarity over the range of  $D_f^*$ ; the differential scour ( $D_f^* - D_i^*$ ) is only a function of the failure length ( $b^*$ ), and does not depend on  $D_f^*$ . Note that the equation is in dimensionless terms, eliminating scale

dependence. Quantitative development of the shape coefficient is described in Chapter 5. Equation 3.7 was used in model calculations to find the lower integration limit of Eq. 3.1.

### 3.3 Cantilever Beam Failure

#### 3.3.1 Unmodified Beam Model

In this section, a model for beam failure is constructed to determine the flexural tensile strength of cohesive soil. It is intended to be calibrated by a simple laboratory procedure evaluating tensile strength as a necessary input parameter for application of the headcut advance model. The model for beam failure is based on a two dimensional cantilever geometry, developed from and modifying the analysis presented by Thorne (1978). Conclusions reached by Ajaz and Parry (1975) are incorporated. Figure 3.5 shows the forces and geometry considered.

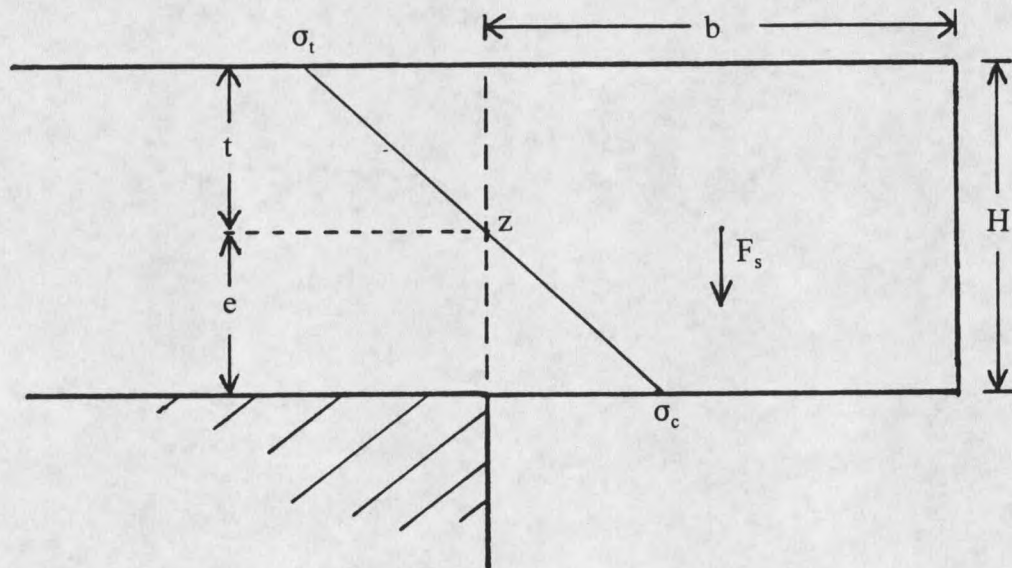


Figure 3.5. Cantilevered Beam Model.

The two fundamental equations used by Thorne, also presented in material mechanics texts, form the basis of the analysis: One equation for the sum of horizontal forces acting on the failure plane, and the second for moments acting about the horizontal neutral axis (z) which lies in the failure plane. The form of these equations is slightly different than Thorne's due to differences in the assumed stress distributions.

$$\Sigma F_x: \quad \frac{1}{2}\sigma_c eL = \frac{1}{2}\sigma_t tL \quad (3.8)$$

$$\Sigma M_z: \quad \gamma_s(HbL)(b/2) = (\sigma_t tL/2)(2t/3) + (\sigma_c eL/2)(2e/3) \quad (3.9)$$

Beer and Johnston (1981) show that the distribution of normal stresses over the cross-section of a beam under transverse load is the same as that for a beam under pure bending forces. This assumes that the distribution of normal stresses over the cross-section is independent of any deformation due to shear stress. Beer and Johnston demonstrate that the longitudinal normal strain in a beam under bending forces varies linearly with the distance from the neutral surface under both plastic and elastic conditions. Given a linear stress-strain relation, this derivation results in a stress distribution also varying linearly from the neutral axis. Consequently, for a beam under transverse loading the maximum tensile stress will exist at the beam surface and will increase with distance between the applied load and the cross-section considered. In the cantilever geometry, the transverse load is generated by the overhanging portion of the beam, and the cross section analyzed is at the point of overhang.

The position of the neutral stress axis has not been specified. Beer and Johnston

(1981) show that for a material with the same stress-strain behavior in both tension and compression, and for a beam with both vertical and horizontal axes of symmetry, that the neutral axis coincides with the horizontal plane of symmetry. Assuming an ideal stress-strain behavior for soils is not justified. However, the results of Ajaz and Parry (1975) make linear stress distributions in tension and compression reasonable. It also is apparent that the beam will fail initially in tension at the upper surface, with maximum compressive stress less than compressive strength at the beam base. Recall that Ajaz and Parry show the compressive strength to be significantly larger than flexural tensile strength. In addition, if the magnitudes of maximum tensile and compressive stress are nearly equal at failure, then the neutral axis must be near the beam vertical midpoint. The ratio of tensile to compressive strengths cannot be used to determine the neutral axis position, as in the derivation by Thorne (1978), because the compressive stress does not approach compressive strength at failure.

With the above reasoning, the limiting parameter for beam stability in the cantilever geometry is flexural tensile strength. Equations 3.8 and 3.9 can be solved for the flexural tensile strength.

$$\sigma_t = \frac{3\gamma_s b^2(1+r)}{2H} \quad (3.10)$$

where  $r = e/t = \sigma_c/\sigma_c$ . Note that the symbol  $\sigma_c$  represents compressive stress at beam failure, a value less than compressive strength. Tensile stress is the limiting stability parameter and thus is equal to tensile strength at beam failure. In Eq. 3.10, the neutral axis position is

controlled by the ratio  $r$  and can be placed anywhere in the failure plane. The lab procedure for beam testing described in Chapter 4 involves measurement of the beam failure length (b) for calculation of the flexural tensile strength according to Eq. 3.10.

Significant assumptions were made in developing this simple cantilever failure model. This makes the relationship calculated between flexural tensile strength and beam failure length semi-empirical. However, one advantage of this approach is that the tensile strength lab procedure places the beam in a geometry identical to that in the headcut experiment. The assumptions made for the simple cantilever failure are valid to the same degree in the headcut failure, so the calculations made for the simple cantilever failure can be directly translated to the more complex headcut case. The proposed lab procedure for calculation of flexural tensile strength is simple and does not allow measurement of the actual stresses or strains involved, but it does produce data which can be used to confidently predict the headcut beam failure length, which is the purpose of the model.

### 3.3.2 Mass Failure of Cohesive Surface Soil

The headcut mass failure model builds on the derivation of simple beam failure in the previous section. The goal is to predict the mass failure length under various soil and hydraulic conditions. In this case, four additional forces acting on the failure slab are considered: weight of surface water ( $F_w$ ), shear force exerted by water flow ( $F_x$ ), tailwater buoyancy ( $F_B$ ), and horizontal tailwater force on the beam face ( $F_T$ ). All forces considered act in two dimensions. Figure 3.6 shows the model geometry. Again, compressive and tensile stresses are assumed to vary linearly from the neutral axis ( $z$ ). Final calculations in

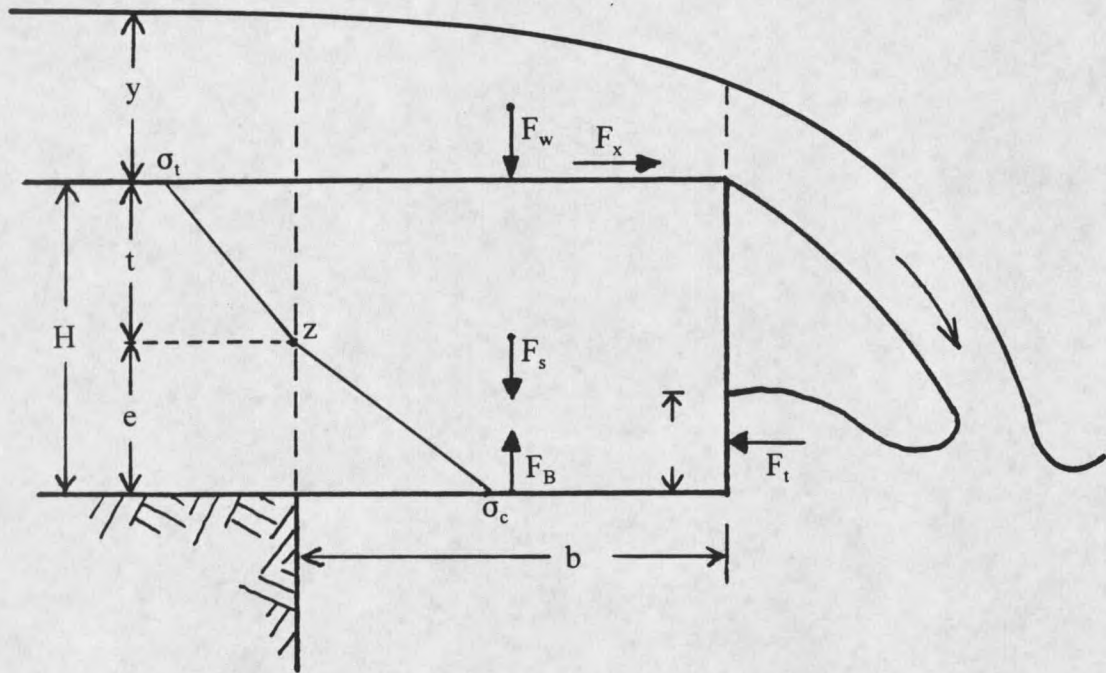


Figure 3.6. Modified Cantilevered Beam Model.

this study presume the beam midpoint as the neutral axis. However, the derivation allows placement of the neutral axis anywhere in the failure plane. Flow depth is assumed constant over the slab length, and equal to the calculated upstream flow depth. Buoyant and horizontal forces exerted by tailwater are considered to be static. Note that the values of maximum compressive stress and maximum tensile stress on the failure plane are not necessarily equal due to the presence of external forces in the longitudinal direction. This means that the stress distribution is linear over the areas of compression and tension individually, but that the respective deformation moduli are not equal. There is consequently an inflection point in the stress distribution at the neutral axis. However, the two external longitudinal forces (surface shear force and horizontal tailwater force) are

small compared to other model forces and act in opposite directions. The resulting difference in model compressive and tensile stresses at failure is also small.

The static force analysis is based on expanded forms of Eqs. 3.8 and 3.9. Variables are as defined in Fig. 3.6, with the exception of  $S$  which is longitudinal bed slope.

Horizontal forces:

$$\frac{1}{2} \sigma_c e + \gamma_w y S b = \frac{1}{2} \sigma_t t + \frac{1}{2} (\gamma_w H_T) H_T \quad (3.11)$$

Solving for compressive stress at failure:

$$\sigma_c = \sigma_t (t/e) + (\gamma_w/e)(H_T^2 - 2ySb) \quad (3.12)$$

Moments about neutral axis:

$$\begin{aligned} \frac{\gamma_s H b^2}{2} + \frac{\gamma_w y b^2}{2} + (\gamma_w y S b) t + \left( \frac{\gamma_w H_T^2}{2} \right) (e - H_T/3) - (\gamma_w b H_T) (b/2) \\ = (\sigma_t/2)(2t/3) + (\sigma_c e/2)(2e/3) \end{aligned} \quad (3.13)$$

Simplifying:

$$\gamma_s H b^2 + \gamma_w [b^2(y - H_T) + 2ySbt + H_T^2(e - H_T/3)] = \frac{2}{3} \sigma_t t^2 + \frac{2}{3} \sigma_c e^2 \quad (3.14)$$

Equation 3.14 can be solved quadratically for the failure length ( $b$ ). Substituting Eq. 3.12 into the last term of Eq. 3.14 gives:

$$\gamma_s H b^2 + \gamma_w [b^2(y - H_T) + 2ySb(t + 2e/3) + H_T^2(e - H_T/3 - 2e/3)] = \frac{2}{3} \sigma_t t^2 + \frac{2}{3} \sigma_t t e \quad (3.15)$$

Rearranging to a quadratic form:

$$[\gamma_s H + \gamma_w (y - H_T)]b^2 + [\gamma_w 2yS(t + 2e/3)]b + [\gamma_w H_T^2(e/3 - H_T/3) - (2\sigma_t/3)(t^2 + te)] = 0 \quad (3.16)$$

Only one root of Eq. 3.16 is physically significant, because  $b$  must be a positive value. As in the simple beam analysis, tensile strength is the limiting parameter for beam stability, and must be determined independently.

### 3.3.3 Dimensionless Cantilever Model

The mass failure model can also be expressed in dimensionless terms. The equivalent of Eq. 3.16 can be derived as:

$$[(1+r)(W_s + Y - T)]F^2 + [2YS(1 + 2r/3)]F + [(T^2/3)(r - T - rT) - 2N/3] = 0 \quad (3.17)$$

Dimensionless parameters are defined as:  $r = e/t$ ,  $Y = y/H$ ,  $F = b/H$ ,  $T = H_t/H$ ,  $W_s = \gamma_s/\gamma_w$ ,  $N = \sigma_t/(\gamma_w H)$ ,  $S = \text{bed slope}$ . A sensitivity analysis was done for the dimensionless model, with results shown in following Figs. 3.7, 3.8, and 3.9. Values of flow depth, neutral axis position, tailwater depth, and soil tensile strength were varied to determine the effect on failure length. Default parameter values for solutions graphed are as follows:  $r = 1.0$ ,  $Y = 0.5$ ,  $T = 0.5$ ,  $W_s = 1.6$ ,  $N = 35$ ,  $S = 0.03$ .

Figure 3.7 shows the change in failure length as neutral axis position is varied from  $r = 0.2$  (near the beam bottom) to 5.0 (near the beam top). The concurrent effect of varying tailwater depth over its extreme range is also shown. Neutral axis position has a dramatic effect on failure length, particularly in the range from  $r = 0.5$  to 1.5 that might be

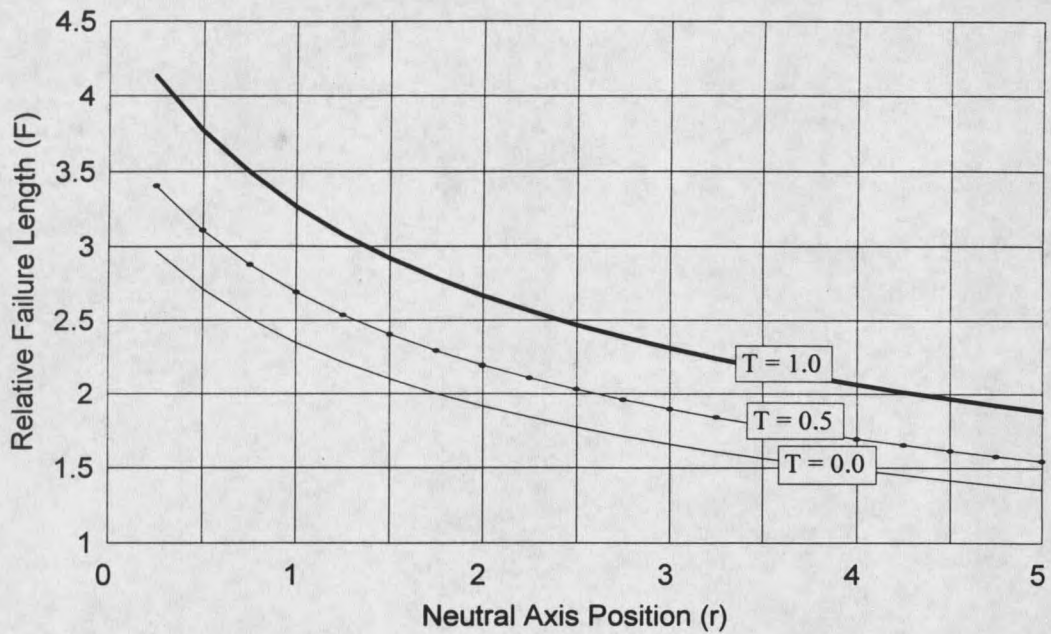


Figure 3.7. Mass Failure Length Sensitivity to Neutral Axis Position.

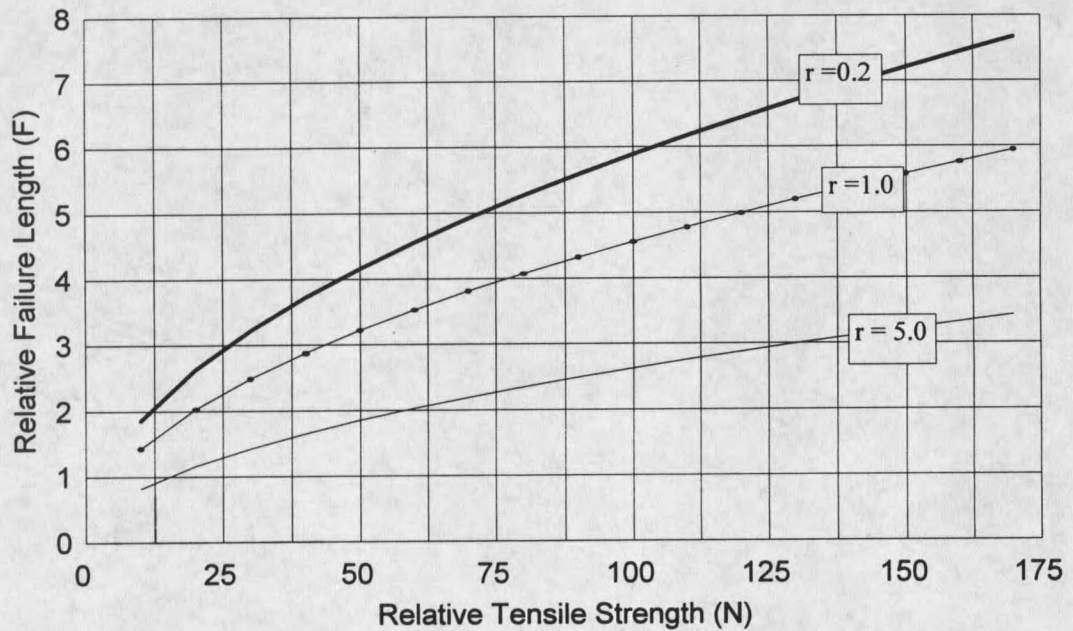


Figure 3.8. Mass Failure Length Sensitivity to Soil Tensile Strength.

considered realistic. Tailwater depth has a smaller impact, with greater depths increasing buoyant force on the beam, resulting in longer failure lengths.

Changes in soil tensile strength, portrayed in Fig. 3.8, have the largest effect on failure length. Failure length increases by over a factor of four as tensile strength goes from 5 to 50 kPa. The equivalent dimensionless tensile range is from 10 to 170. Tensile strength values determined for physical modeling runs described in Chapter 5 range from 8 to 12 kPa ( $N = 27$  to 65).

Figure 3.9 shows variation in relative flow depth from 0.5 to 5.0, with the most significant impact on failure length occurring over small flow depths. It should be noted

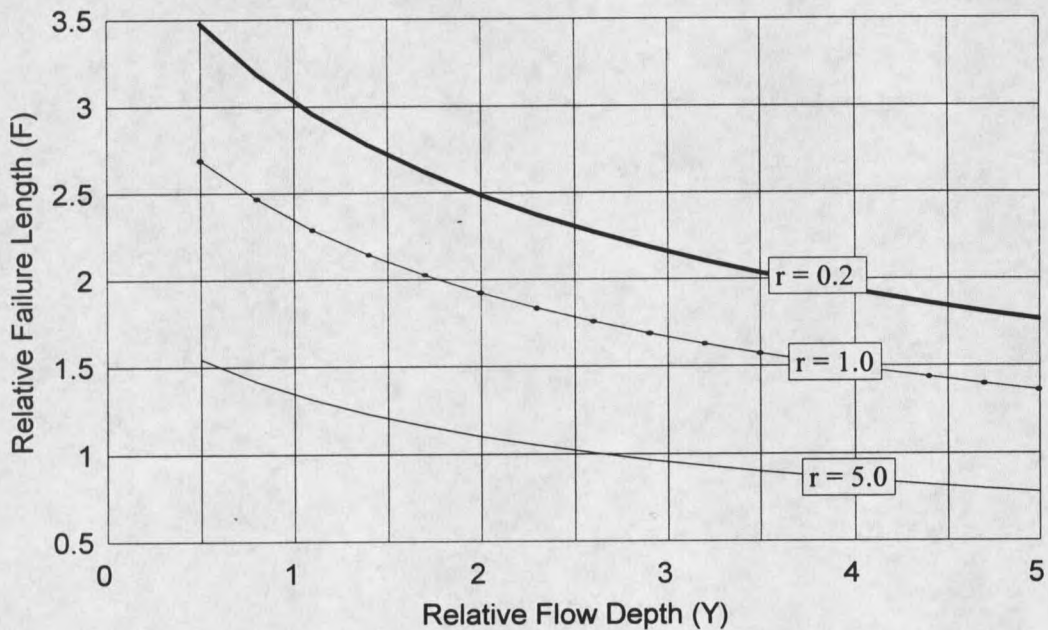


Figure 3.9. Mass Failure Length Sensitivity to Flow Depth.

that flow detachment at the headcut brink will only occur for relative flow depths of approximately 1.0 or smaller.

### 3.4 Integrated Advance Rate Model

The headcut advance rate equation combines the cantilever mass failure model and the base layer scour model. The first determines the length scale of the advance rate and the second dictates the time scale. Scour calculations depend on the mass failure length, so the two models are not entirely independent. Advance rate is calculated over a single failure cycle, predicting linear headcut movement upstream in discrete steps. Each step is marked by a mass failure event of the surface layer. For each failure cycle the advance rate  $dx/dt$  is:

$$dx/dt = \frac{b}{\Delta T^* T_r} \quad (3.18)$$

Values of  $b$  (mass failure length) and  $\Delta T^*$  (dimensionless cycle period) are calculated according to Eqs. 3.16 and 3.1 respectively. Reference time  $T_r$  dimensionalizes the denominator and is calculated through Eq. 2.31. The following chapters describe work done to calibrate this equation with physical model data.

## CHAPTER FOUR

### 4. MATERIALS AND METHODS

This chapter describes the equipment, methods, and materials used in the laboratory experiments. All experiments were conducted in the Hydraulics & Fluid Mechanics and Bulk Materials laboratories of the Civil Engineering Department at Montana State University, Bozeman. Experiments were done for three separate elements of the research. The first, referred to as fixed overfall runs, involved model calibration for the vertical rate and equilibrium depth of scour hole formation in non-cohesive sediment, and are numbered runs SH1 through SH4. These experiments also included an investigation of the scour hole profile shape. The second set of experiments was done to validate the proposed headcut retreat model in layered sediments, numbered runs CL1 through CL9 and referred to as retreating headcut runs. The mass failure of an overlying cohesive layer was observed to test the cantilevered slab model, and the mechanism of scour of the underlying sand bed was examined. The last experiments tested the simple cantilevered slab failure model under controlled conditions to determine the value of flexural tensile strength of cohesive soil. In addition to providing data for the present experiments, a second goal of these tests was to develop the basis for a practical method for measuring tensile strength of various soils.

#### 4.1 The Flume

Fixed overfall and retreating headcut experiments were conducted in a plexiglass flume designed and constructed specifically for this research. Figure 4.1 shows a longitudinal cross-section of the flume. The inside dimensions of the flume are 241 cm long, 15.2 cm wide, and 61 cm deep. The side walls are  $\frac{1}{2}$  inch clear plexiglass, allowing an unimpeded view of the contents in two dimensions. Sheets of translucent 1 mm grid paper are adhered to one wall for data collection. These sheets were scaled from an origin point at the flume inlet base; any point over the flume length and depth could be accurately determined in two dimensions. To allow adjustable inlet and outlet heights, the flume end plates are cut down. At the flume inlet a separate headtank can be attached and adjusted vertically to set the inflow height. The headtank dimensions are 12.7 cm long, 15.2 cm wide, and 50.8 cm deep. Flow enters the bottom of the headtank and passes upward through a layer of heavy gravel to improve uniformity. The headtank overflow edge is rounded for a smooth flow transition into the flume. At the flume discharge, an adjustable spillway can be attached to control the exit water level.

A false floor is placed on the flume bottom with three channels routed on the base side running the length of the flume. The channels lie between the false floor and the structural floor and are approximately 5 mm deep and 20 mm wide. Small holes are drilled in the false bottom along the length of these channels to allow water passage upward into the flume and to provide a drainage path. At the discharge end of the flume a port is placed which leads to an inlet plenum connecting the false bottom channels. The purpose of this

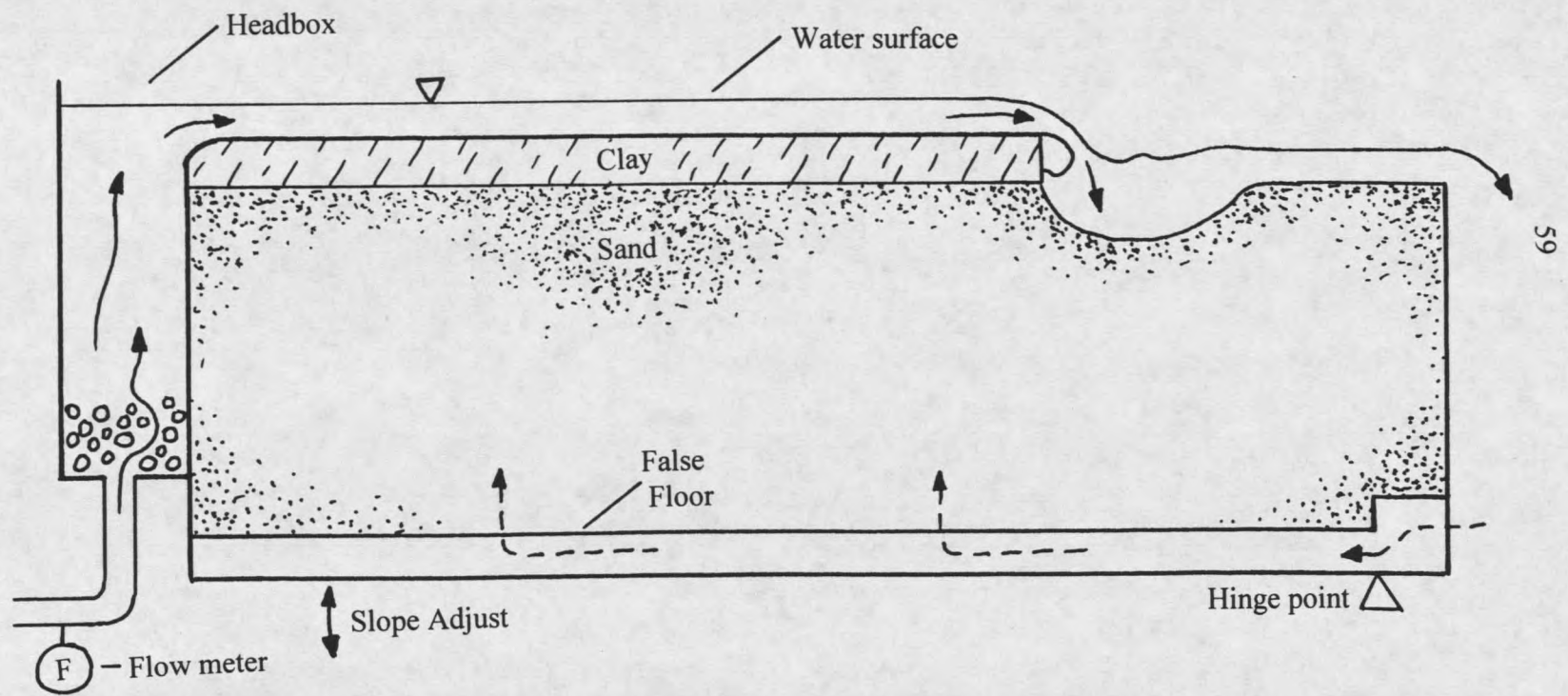


Figure 4.1. Flume Longitudinal Cross-Section (not to scale).

mechanism is to allow the flume contents to be saturated slowly from the bottom upward by controlling the applied head. This ensures that the contained soil is completely and uniformly wetted. All experiments were conducted under saturated conditions.

The discharge end of the flume support table is hinged to allow inclination at any angle. At the opposite end, a hydraulic jack is positioned to adjust the flume slope.

A paddlewheel flowmeter was placed on the inlet side of the flume headbox. The flowmeter produces a sinusoidal output signal with amplitude and frequency proportional to the flow rate. The AC signal was converted to DC via a simple diode bridge, and the output voltage measured with a digital voltmeter. A calibration curve was constructed over the full experimental flow range with reasonable accuracy. The flowmeter was used for all fixed overfall runs and the first retreating headcut run. For several of these runs the flow was also measured manually as a backup to the flowmeter.

For all retreating headcut runs except CL2, flow rate was measured manually with a seventy gallon container placed to catch the flume discharge flow. The container was placed on a scale and used with a digital stopwatch for the measurements. It was possible to collect several hundred pounds of water per measurement, minimizing any error caused by the weight of entrained sand or clay. Water temperature was recorded for each run.

The duration of the fixed overfall experiments approached 24 hours, making it necessary to have a reliable constant head water source for a steady flow rate. For all but the first run (SH1), a constant head tank was used to supply the flume. This proved very successful, but provided a limited flow due to the constrained elevation of the tank. A tap connected to the city water supply was used as a source for runs SH1 and CL2. For all

subsequent retreating headcut runs, flume inlet flow was provided by a small centrifugal pump taking suction on a sump tank. Flume discharge flow was directed back to the sump tank, keeping the pump inlet head constant. Flow was varied by means of a throttle valve at the pump discharge. No measurable variation in flow rate was noted during these experiments.

#### 4.2 Sand and Clay Materials

The same sand and clay was used in all experiments. The sand is F-70 Ottawa sand, with a dry bulk density of  $1651 \text{ kg/m}^3$  and a mean particle diameter ( $d_{50}$ ) of  $0.20 \text{ mm}$ . Particle size distribution is shown in Fig. 4.2. The angle of repose, as measured directly

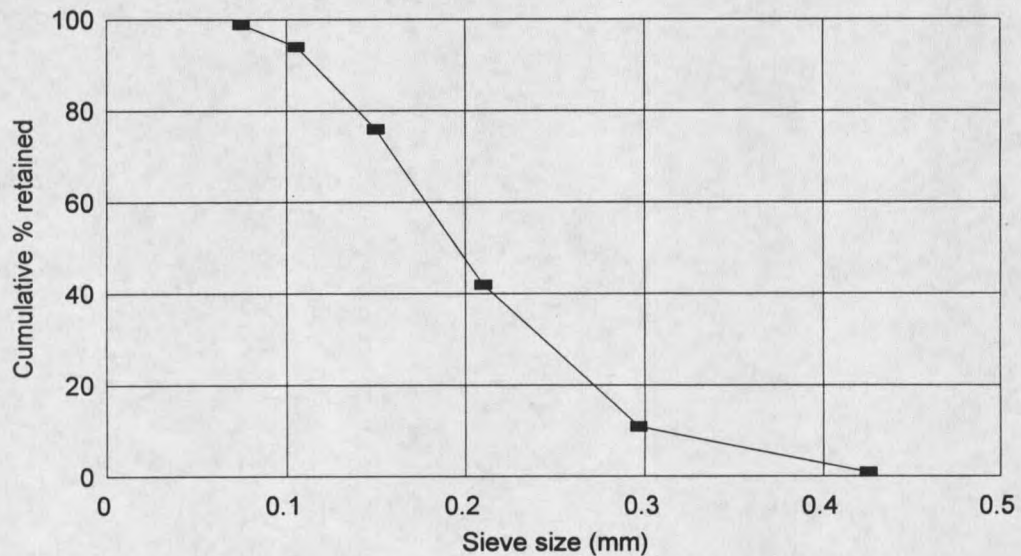


Figure 4.2. Ottawa sand particle size distribution.

in the flume, was taken as  $30.3$  degrees. A particle density of  $2650 \text{ kg/m}^3$  was used in calculations, corresponding to quartz materials.

Pure China White clay was used as the cohesive soil. It is a kaolinite clay with a specific gravity of 2.66. The clay was prepared with a moisture content of 100% prior to consolidation for all experiments. Both sand and clay were kept continuously saturated during run preparation and data collection. This would tend to minimize any variation in erosion resistance or other mechanical properties due to changes in the amount or rate of change of the interparticle liquid phase. Surface erosion of the clay was minimal, appearing almost non-existent, during layered soil runs.

Clay moisture content and bulk density, both a function of consolidation, were chosen as the primary experimental variables. Several sources including Ajaz and Parry (1975) and Thorne (1988) reference moisture content as a primary factor influencing tensile strength, which is of fundamental interest in this study.

#### 4.3 Fixed Overfall Experiments

This series of experiments was designed to isolate scour hole formation without a retreating headcut. Data from these runs were used to calibrate models for the rate of scour in the vertical direction and for the predicted equilibrium scour hole depth in the Ottawa sand. Because the rate of horizontal scour at the original sand level was of interest, it was also necessary to investigate the shape of the scour hole profile. All runs used a fixed overfall position for controlled scour hole formation and were allowed to progress until equilibrium was reached. (Run SH2 was unfortunately terminated prior to equilibrium.) Four runs were completed, with varying flow rates and slightly varying slopes (3.0 to 3.5 percent).

To set up the scour hole runs, dry sand was first placed in the drained flume. Sand from previous runs was not removed from the flume, but was distributed evenly over the flume length. New sand was added in layers. Each layer was consolidated by vigorously hitting the flume wall with a length of 2 by 4 board. When the sand reached the desired level, it was saturated from the bottom by applying an increasing head in discrete increments over a minimum period of 12 hours. The surface of the saturated sand was then reduced to a constant level with a scraper designed for this purpose. A tightly fitting plexiglass plate was placed over the upstream reach of the flume on top of the sand, for a distance of 128 cm from the head tank overflow. Flow from the head tank passed over the top of this plate to the overfall position. The plate was carefully leveled to ensure a uniform flow depth and slope, then fixed in place by tightening large "C" clamps on the flume walls. Flow leakage around the plate was prevented with a thin film of Vaseline spread along the edges.

At the overfall, the headcut was formed by removing the downstream sand to the correct level and adjusting the discharge spillway to the same level. A headcut height of 4.0 cm was used for all scour hole runs. A piece of smooth styrofoam was placed upstream of the discharge with its surface at the same level as the initial sand. This ensured uniform downstream flow conditions and controlled the overfall height throughout the scour hole formation.

Finally, a 35 mm camera was positioned opposite the gridded flume wall for data collection. An automatic timer allowed exposures to be taken at variable intervals. Time zero was defined as the point of initial flow impingement at the overfall; photos were taken

at 5 second intervals over the initial minute of rapid hole development. The exposure interval was then increased regularly to a maximum of one or two hours near the end of the run. Scour hole run duration varied from 15 to 23 hours, with the exception of run SH2 which was terminated at 6 hours. A digital stopwatch fixed to the flume sidewall determined photo exposure times over the run. Data was extracted from the still photos which clearly show the scaled wall grid and two dimensional scour hole profile. Points on the profile could be determined to within 2 mm.

#### 4.4 Retreating Headcut Experiments

This experiment series was used to calibrate the integrated headcut advance model. Two soil layers of constant thickness were placed in the flume. The thickness and moisture content of the surface layer were varied over the run series, as well as the headcut height and flow rate.

Ottawa sand was used as the base layer; it was placed in the flume and saturated in the same manner as for fixed overall runs. The sand surface was leveled and smoothed with particular care because any variation would affect the overlying clay layer.

To form the cohesive surface layer, dry clay was first mixed with water in measured amounts in a separate container. A mechanical mixer was used for the larger amounts required for thick layers, while smaller amounts were mixed by hand. Mixing was continued until the clay slurry was of uniform consistency with no inclusions. At a moisture content of 100% the clay was nearly fluid, making it easy to place and distribute evenly over the sand without disturbing the base layer. Care was taken to prevent air

bubbles from remaining in and around the clay layer as it was added to the flume. With the clay in the flume, the surface was again leveled, giving the clay a constant thickness throughout the flume prior to consolidation. Clay mixing and placement were done quickly to prevent dehydration as much as possible.

To lower the moisture content, the clay layer had to be consolidated. The flume was designed with a steel I-beam which fits evenly within the inside dimensions of the flume. Two layers of cotton sheeting were placed between the clay and the I-beam to prevent adherence and allow subsequent beam removal without disturbing the consolidated clay. With some experience, it was possible to achieve a very smooth clay surface following consolidation. To achieve consolidation, weights were placed on the I-beam in positions balanced laterally and longitudinally. Weights were added in increments to facilitate even consolidation. The loading period varied from three to five days to ensure equilibrium settling. Over this time the sand base layer was kept saturated by applying an even head via the base plate to a level just below the sand surface, making up for flume leakage. No settling of the sand surface was detectable during clay consolidation. Lateral bowing of the flume walls was prevented by steel angle iron placed around the perimeter of each wall and clamped. With this support, the flume was able to carry consolidating loads over 2000 pounds without catastrophic failure. When consolidation was complete the load and I-beam were carefully removed, leaving the clay layer of uniform thickness and moisture content.

After removal of the consolidation load, the remaining set-up procedure and data collection were conducted immediately to prevent desiccation effects on the surface layer.

Up to the run start time, the clay was kept covered with moist cloth or plastic wrap. Two or three clay samples were taken for moisture content determination without disturbing the reach used for data collection. The samples were oven dried for moisture content calculation. The initial headcut was pre-formed by removing clay and sand to the desired overfall depth over a short downstream reach. This section was then leveled. For runs CL8 and CL9 the overfall height was greater than the clay layer thickness. A layer of sand was removed over the downstream reach as well as the clay. This was done to enhance formation of a well developed, free falling jet. The flume discharge spillway was adjusted vertically to the same level as the downstream soil, thus controlling the tailwater depth and overfall height throughout the run.

Data for the retreating headcut runs was recorded primarily by direct observation. The parameters of most interest were the longitudinal position and time of mass failure events and the depth of maximum base layer scour. The dynamics of the headcut advance could also be clearly viewed in two dimensions from the ungridded side of the flume. Runs CL7 through CL9 were videotaped from that vantage for later review, which proved to be very useful.

The minimum length of the data collection reach was 82 cm for runs CL6 and CL7, while remaining data sets covered 120 to 146 cm. Initial headcut position for all runs but CL2 and CL7 was between 189 and 196 cm on the longitudinal scale where the flume discharge point is at 245 cm. Runs CL2 and CL7 were initiated respectively at 155 cm and 106 cm on the same scale.

#### 4.5 Cantilevered Beam Failure

Soil tensile strength was determined to be a fundamental parameter required for the cantilevered beam failure model. A series of experiments involving simple beam failure were conducted to calculate the tensile strength of the clay used in this study. Because there is not an abundance of data on soil tensile strength, a second goal of these experiments was to test the procedure as a practical method of measuring flexural tensile strength of various cohesive soils.

A rectangular box was designed and constructed for the experiments. Box design was simple but required very precise assembly. Inside dimensions of the box were 15.2cm by 61.0 cm and 17 cm deep. It was constructed of plexiglass, although any rigid impermeable material could be used. All pieces of the box were connected with screw bolts, and without adhesive, allowing for easy disassembly. The top plate was unattached and machined to slide easily but with very small clearance from top to bottom of the box. Handles were attached to the top plate for easy handling, and 1mm holes were drilled in an even pattern with approximately one inch spacing over the plate.

To form the clay slab, measured amounts of clay and water were mixed to a homogenous consistency. As in the flume runs, an equal mass of dry clay and water was used for the initial mixture for all experiments. Before adding the clay, a piece of cotton sheeting cut to the inside box dimensions was placed evenly on the box bottom. The sheet had one long end which extended beyond the end of the box, fitted through the junction between the base and end plates. Clay was placed over the cotton sheet in an even layer,

again with care to prevent inclusion of air bubbles. Over the clay a double layer of cotton sheeting was placed, cut to the inside box dimensions. After the sheeting, the plexiglass top plate was placed on the clay surface. The top sheeting layer served two functions: to prevent clay adherence to the top plate, and to provide a conductive path for water escape through the top plate holes during consolidation.

With the top plate in place, weights were added in a centered pattern for uniform consolidation. A scale system was devised to ensure even consolidation and a resulting uniform clay thickness. Weight was added in increments to the desired consolidation pressure and allowed to settle for a minimum of 36 hours. At this point no further consolidation was apparent, and the load was removed.

For data collection, the box was disassembled with care to prevent clay disturbance. The well-formed clay slab then remained lying on the base plate. Slab thickness was measured and recorded at frequent intervals around the slab perimeter. The consolidation procedure limited thickness variations to less than 2mm. Using the bottom cotton sheeting scrolled on a dowel, the clay layer was then pulled slowly off the bottom plate longitudinally. This placed the unsupported end of the clay slab in a cantilevered beam geometry. A profile view is shown in Fig. 4.3. Cantilever length was slowly increased until tension cracks appeared, leading to beam failure at the base plate edge. The failure length was recorded and the process repeated over the length of the slab, with failure events occurring at regular intervals. The derivation of tensile strength as a function of failure length is described in section 3.3.1. Depending on slab thickness, between four and six failures were recorded for each data set.

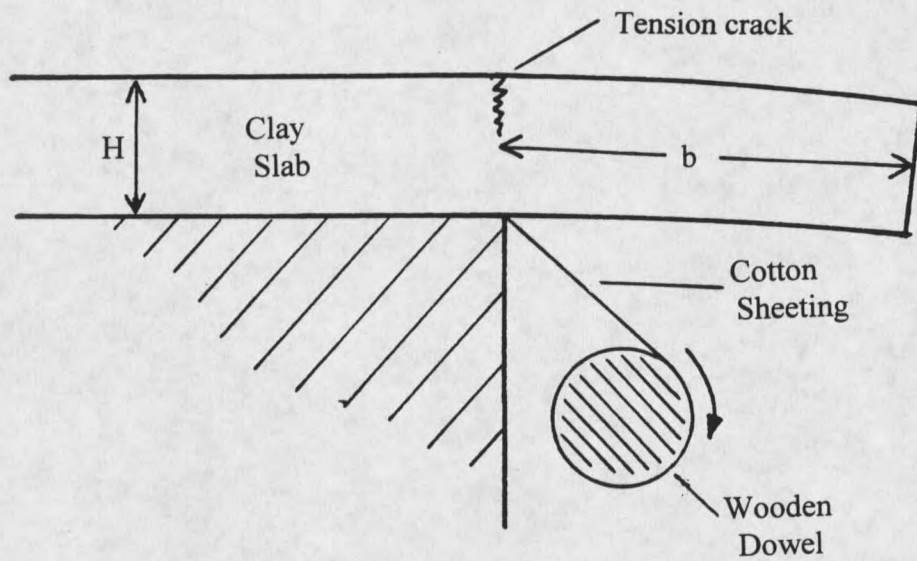


Figure 4.3. Profile View of Cantilevered Beam Experiment.

Moisture content samples were taken at opposite ends of the clay slab and also at intermediate points in some cases. Eight data sets were collected over a range of moisture contents, as controlled by consolidation pressure.

## CHAPTER FIVE

### 5. RESULTS AND DISCUSSION

This chapter presents the results of experiments described in Chapter 4. Three sets of experiments were completed: flume runs for fixed overfall and retreating headcut cases, and cantilevered beam failure analysis. Flume experiments were done with the end goal of evaluating the two layer headcut advance model. This involved separate calibrations of sediment scour equations and the surface layer mass failure model. The cantilevered beam experiment series was conducted independently to determine cohesive soil tensile strength for input to the headcut advance model.

#### 5.1 Physical Modeling

##### 5.1.1 Fixed Overfall Experiments

Four fixed overfall runs were conducted (SH1-SH4) to examine stable scour hole formation at an unchanging surface impingement point. The primary parameter varied was flow discharge, ranging from 0.0020 to 0.0029 m<sup>2</sup>/s. All runs were conducted with a 4 cm overfall drop height and bed slope of 3.0 to 3.5%. Reynolds number varied from 1333 to 1907, and Froude number from 2.58 to 2.91, indicating turbulent supercritical conditions for normal flow upstream of the overfall. Values of hydraulic parameters are based on Eqs.

2.13 through 2.20. Table 5.1 shows fundamental parameter values for the fixed overfall runs.

Table 5.1. Fixed overfall experimental parameters.

Run	q (m <sup>2</sup> /s)	S (m/m)	h <sub>n</sub> (m)	Re	F <sub>r</sub>	D <sub>h</sub> (m)
SH1	0.0027	0.03	0.0047	1827	2.68	0.04
SH2	0.0020	0.03	0.0039	1333	2.58	0.04
SH3	0.0029	0.035	0.0046	1907	2.91	0.04
SH4	0.0029	0.03	0.0049	1907	2.70	0.04

All runs were allowed to progress to equilibrium depth with the exception of run SH2, which was terminated at 6.5 hours.

#### 5.1.2 Retreating Headcut Experiments

Nine total retreating headcut runs were completed, numbered CL1 through CL9. Only six runs yielded useable data. Three of the first four runs were unsuccessful due to inadequate water pressure and excessive disturbance of the clay layer during the consolidation process. Successful data sets were used to calibrate the empirical geometry coefficients introduced in Chapter 3 and to evaluate the final headcut advance rate equation.

Fundamental parameters of the retreating headcut runs are summarized in Table 5.2. The primary parameters varied were discharge rate (q), clay layer thickness (H), and headcut height (D<sub>h</sub>). All runs were conducted at 3% bed slope, with turbulent, supercritical

flow over the upstream reach. Clay consolidation pressure was varied only for run CL8, and clay moisture content was stable over all data sets, varying from 0.645 to 0.678. Lowering the moisture content further was limited by the excessive weight required for consolidation. The values of hydraulic parameters were calculated in the same manner as

Table 5.2. Retreating headcut experimental parameters.

Run	CL2	CL5	CL6	CL7	CL8	CL9
q (m <sup>2</sup> /s)	0.0089	0.0133	0.0070	0.0114	0.0089	0.0097
H (cm)	3.2	4.3	1.3	1.3	1.3	2.9
D <sub>h</sub> (cm)	3.2	4.3	1.3	1.3	3.8	3.9
S	0.03	0.03	0.03	0.03	0.03	0.03
Re	5933	12091	7000	11400	8780	9690
F <sub>r</sub>	3.11	3.40	3.17	3.37	3.26	3.31
Consolid.	20.03	20.00	20.00	20.00	25.80	20.00
Press.(kPa)						

for fixed overfall runs, according to Eqs. 2.13 - 2.20. The equations for equilibrium scour depth and scour rate were used as calibrated for the Ottawa sand in fixed overfall runs.

## 5.2 Base Layer Scour

### 5.2.1 Calibration of Equilibrium Scour Depth Equation

Fixed overfall runs were used to calibrate the equilibrium scour depth Eq. 2.29 for the Ottawa sand. Two terms in the expression for equilibrium diffusion length, Eq. 2.28, were modified from the suggested values given by Bormann and Julien (1991). The

downstream face slope angle  $\alpha$  is assumed equal to the jet tailwater entry angle  $\chi$  in their studies. After observation of current scour hole formation experiments, a value of  $\alpha$  equal to the sediment angle of repose  $\phi$  (30.3 degrees) seemed a better assumption. For the depths predicted in this study this difference in assumptions had a significant impact, since the values of  $\phi$  and  $\chi$  were distinctly different. Jet entry angles varied from 53.8 to 58.8 degrees for fixed overfall runs.

Secondly, the value of the local friction parameter,  $B$ , was varied to fit the equation to observed data. Bogardi (1974) uses the coefficient  $B$  to relate the local friction coefficient  $C_f$  to surface roughness according to Eq. 2.8. This parameter also affects the fit of the scour rate equations, as the equilibrium depth is used as a normalizing parameter. Bormann and Julien (1991) employ a value of  $B = 2.0$  in their work. For the present data, best results were obtained with  $B = 2.3$ , which is well within the range 2.0 - 2.9 referenced by Bormann and Julien. Values of predicted and observed equilibrium scour depths for fixed overfall runs are given in Table 5.3. Recall that run SH2 was abbreviated before equilibrium conditions were reached.

Table 5.3. Equilibrium scour depth for fixed overfall runs.

Run	SH1	SH2	SH3	SH4
$D_e$ observed (m)	0.184	0.114	0.197	0.193
$D_e$ predicted (m)	0.190	0.157	0.194	0.194
Run time (hr)	15.0	6.5	21.4	23.0

The final form of the equilibrium depth model is given as Eq. 2.29. Tailwater depth

was assumed negligible in this study. An observation on the form of Eq. 2.29 should be made. The value of  $D_e$  is based on the assumption of a linear jet trajectory following tailwater entry, represented by the  $\sin \chi$  term. Analysis of the jet trajectories in this study suggest that the tailwater entry angle is not a good approximation for the trajectory through the plunge pool. Equation 2.29 successfully predicts the scour depths observed, but this seems qualified by the difference between actual and assumed trajectory angles. Analysis of the trajectory is described in detail later in this chapter.

### 5.2.2 Scour Rate Model Calibration

Fixed overfall runs were also used to calibrate the vertical scour rate model for the Ottawa sand, concurrently with equilibrium scour depth. The model was developed by Stein et al. (1993) and is expressed in Eqs. 2.30 and 2.32. Two variables were used to fit the model to physical data: the excess shear coefficient  $\kappa$  in Eq. 2.6, and the local friction parameter  $B$ . The local friction parameter affects the scour rate only indirectly through the normalizing parameter  $D_e$ . The shear coefficient relates the sediment mass removal rate from a unit surface area to the excess shear stress applied. The values of remaining constants are the same as used by Stein et al. (1993). These include the jet diffusion coefficient ( $C_d = 2.6$ ), and excess shear equation exponent ( $\xi = 1.5$ ). The form of the scour rate equation depends on the excess shear exponent, with three separate solutions given by Stein et al. (1993). The value of 1.5 for  $\xi$ , proposed by Foster et al. (1977), is based on non-cohesive sediment transport equations. The scour equation form used for this study is for an excess shear exponent of 1.5.

Critical shear stress was not allowed to vary as an independent parameter, but was calculated using Eq. 2.33. Resulting values were consistent over the four data sets, averaging 0.36 Pa. This agrees well with the value of 0.35 Pa given for a slightly finer sand ( $d_{50} = 0.15\text{mm}$ ) by Stein et al. (1993). The local friction coefficient  $C_f$  was determined by the Blasius equation (2.11), also used by Stein (1990). Table 5.4 shows model parameters calculated for runs SH1-SH4, including potential core depth  $D_p$ , potential core scour time  $t_p$ , and jet impingement angle  $\chi$ .

Table 5.4. Scour model parameters for fixed overfall runs.

Run	$\chi$ (deg)	$D_p$ (m)	$D_p^*$	$D_e$ (m)	$t_p$ (sec)	$T_p^*$	$T_r$ (sec)
SH1	55.4	0.014	0.07	0.189	14.4	0.002	8358
SH2	58.8	0.011	0.07	0.157	11.2	0.002	7427*
SH3	53.8	0.014	0.07	0.194	13.8	0.002	8494
SH4	55.0	0.015	0.08	0.194	14.9	0.002	8494

Figure 5.1 shows the predicted and observed scour depths as a function of time, in dimensionless form. Equations 2.30 and 2.32 were used to calculate the model curve. Parameters  $\kappa$  and  $B$  were then varied to produce the best data fit for both equilibrium depth and scour rate, with resulting values of  $B = 2.3$  and  $\kappa = 0.17$ . The value of  $\kappa = 0.30$  given by Stein et al. (1993) for fine sand is slightly higher than determined in this study. However, the model is fairly sensitive to this parameter;  $\kappa = 0.30$  fits data for run SH1 well, whereas  $\kappa = 0.13$  better represents runs SH2 and SH4. The model predicts the scour rate

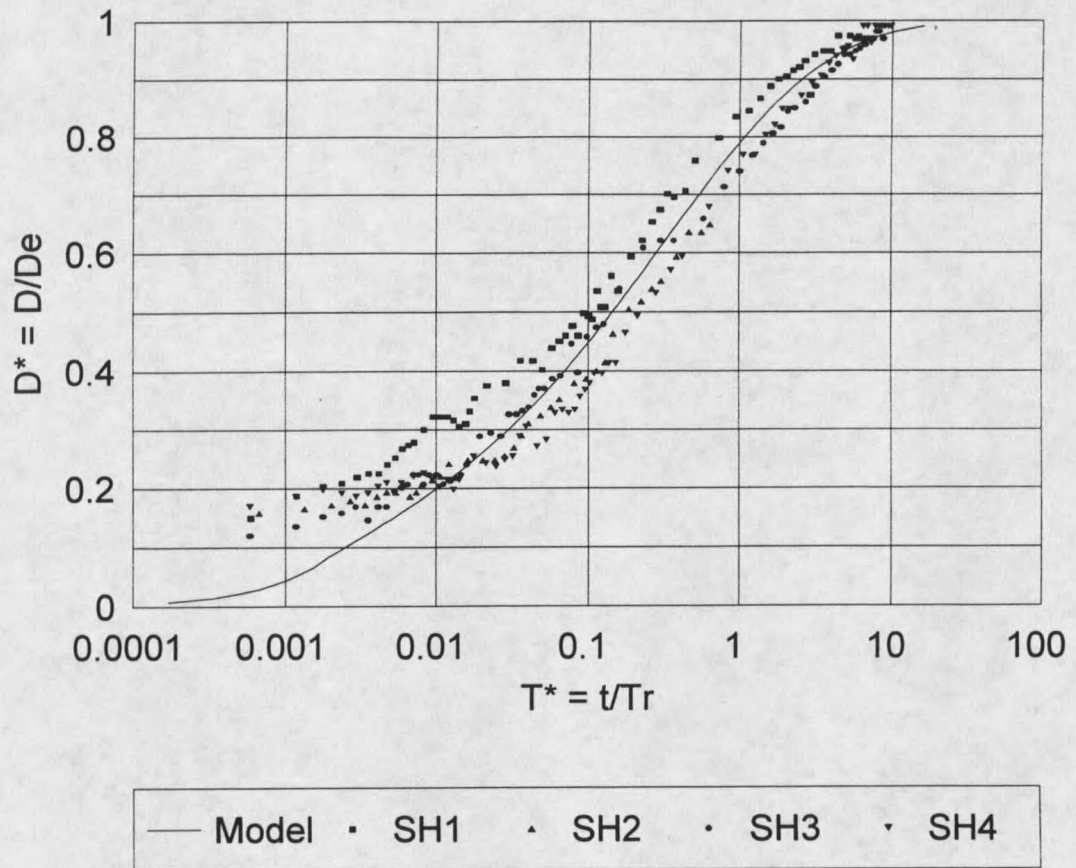


Figure 5.1. Scour Depth With Time for Fixed Overfall Runs.

well over most of the hole formation. Small scour depths over the initial period ( $T^* < 0.01$ ) are somewhat underpredicted, but this translates to a very short period of time on a linear scale. The longest period corresponding to a  $T^*$  value of 0.01 is less than 3 minutes for the fixed overfall runs.

### 5.2.3 Jet Trajectory

The trajectory of the submerged jet in the plunge pool is a critical factor controlling scour hole geometry. The trajectories observed in fixed overfall runs were examined and

used with data from retreating headcut runs to model the trajectory angle.

The assumption made in virtually all scour studies including those by Bormann and Julien (1991) and Stein et al. (1993), is that the jet impinges at a horizontal distance  $X_n$  from the overfall face, entering the tailwater at an angle  $\chi$  and continuing in a linear submerged trajectory at the same angle. Because the jet is neutrally buoyant this would seem warranted, but does not consider other forces that may act on the jet, as noted by the above researchers. Stein remarks in his dissertation (1990) that the maximum scour point, located on the jet centerline, is consistently displaced in the upstream direction for fixed overfall experiments.

Figures 5.2 through 5.5 show the trajectories observed for runs SH1 through SH4, plotted from an origin at the tailwater impingement point  $X_n$ . Several different model lines are plotted for comparison: the linear trajectory described above, the best fit linear regression line (constrained through the calculated impingement point), and a free fall trajectory in air projected beyond the water surface. There is obviously considerable experimental scatter in the trajectory angle for any given run. One main characteristic is consistent, however; at later times, when the scour hole is relatively deep, the maximum scour point is well upstream of the linear trajectory model. In runs SH2 and SH4 the trajectory is actually bent past the vertical over a small portion of the hole depth. The linear regression lines are used in development of the jet refraction coefficient  $C_r$ .

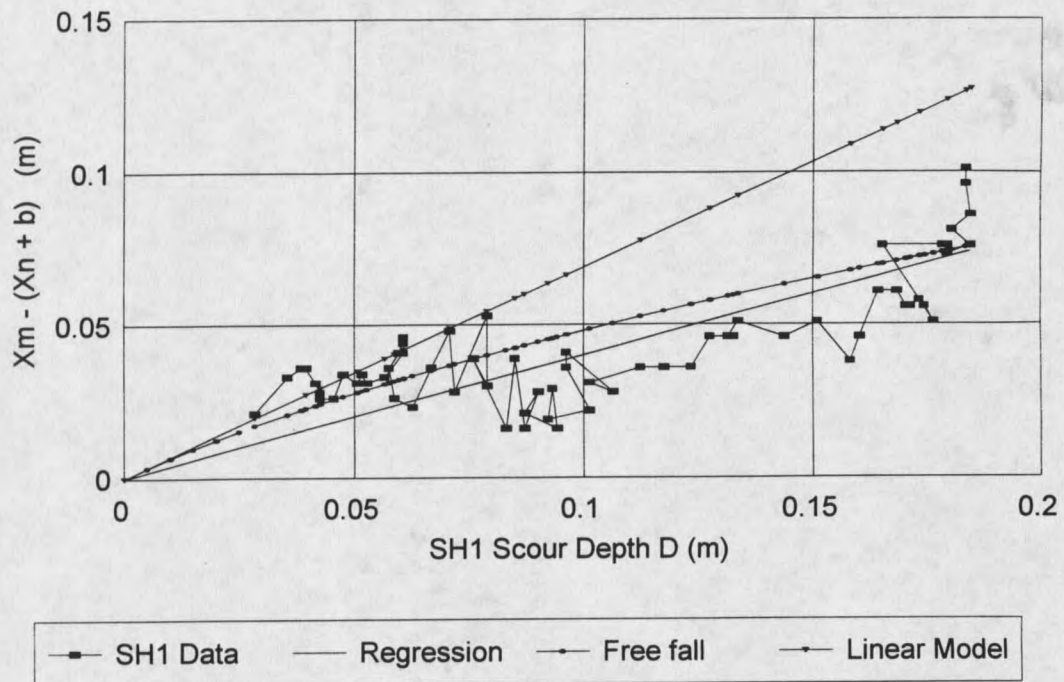


Figure 5.2. Run SH1 Submerged Jet Trajectories.

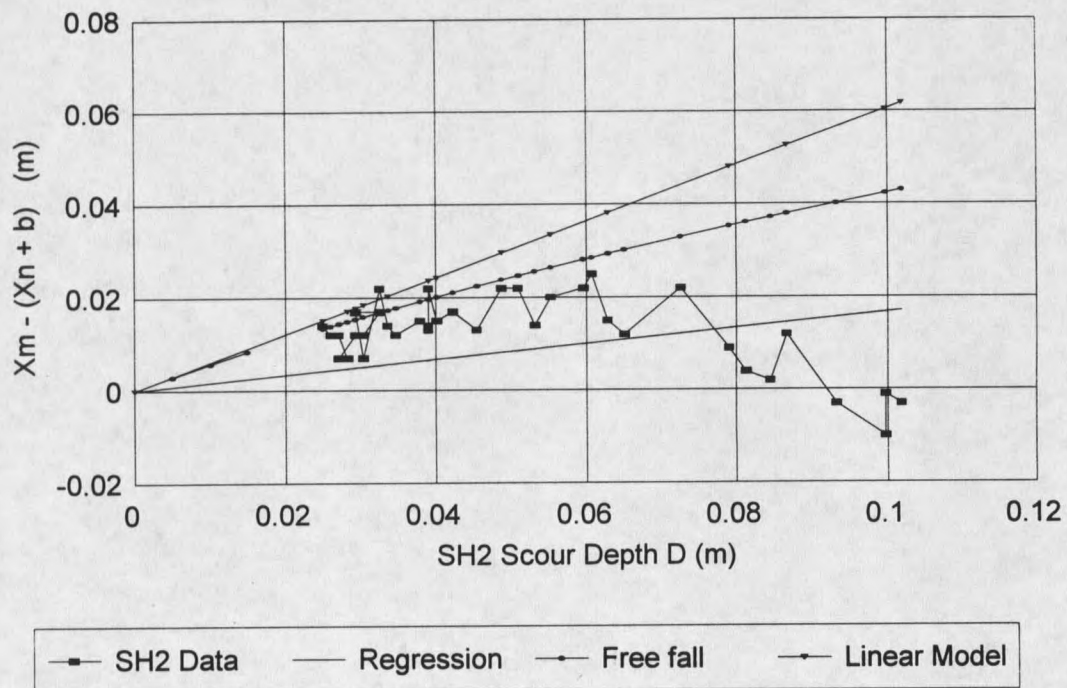


Figure 5.3. Run SH2 Submerged Jet Trajectories.

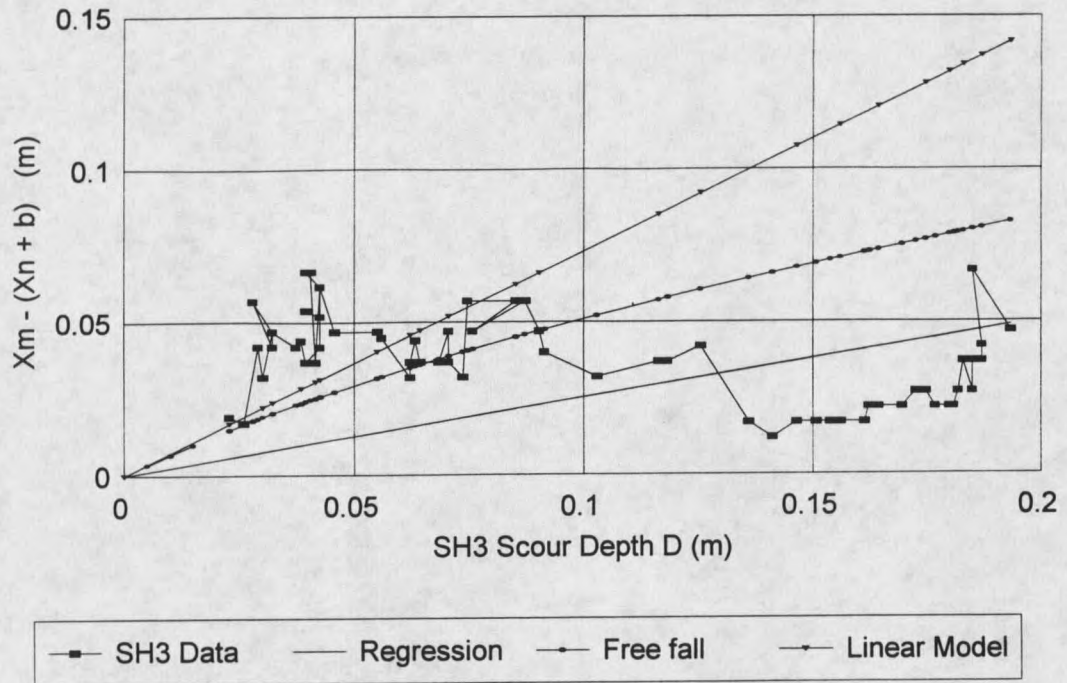


Figure 5.4. Run SH3 Submerged Jet Trajectories.

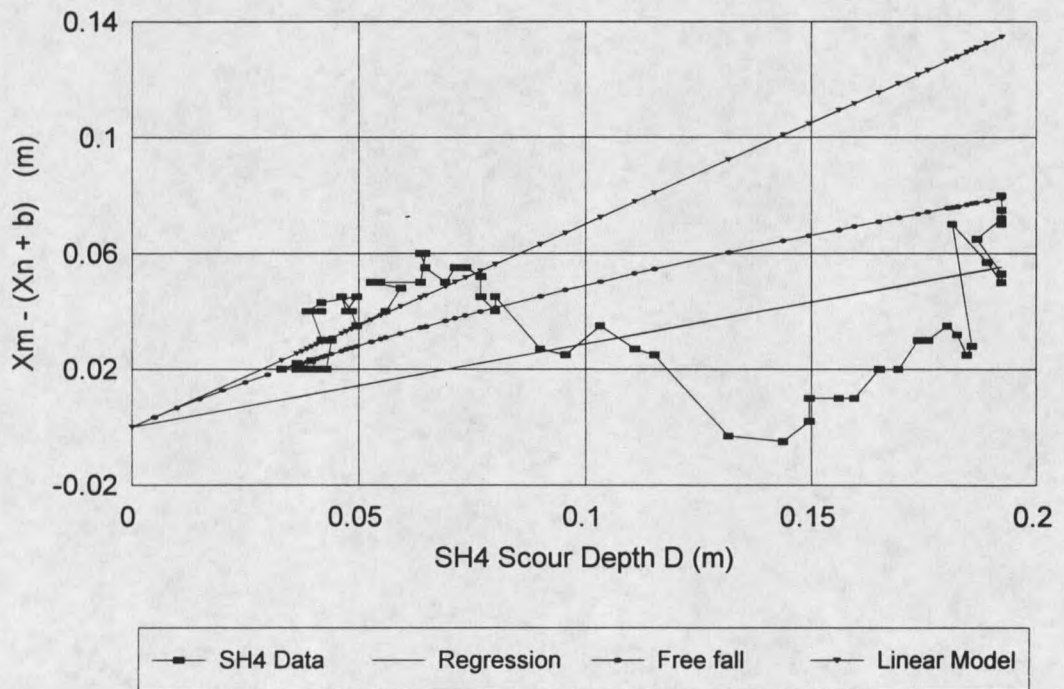


Figure 5.5. Run SH4 Submerged Jet Trajectories.

#### 5.2.4 Calibration of Trajectory Refraction Coefficient

As introduced in section 3.2.4, the angle of the submerged jet trajectory in the scour hole influences the final scour depth  $D_f$ . In both fixed overfall and retreating headcut runs, the observed trajectories were steeper than predicted by extension of the tailwater entry angle. An empirical refraction coefficient  $C_r$  was defined as the ratio of the submerged jet angle to the tailwater entry angle in Eq. 3.6. Two independent methods were used to quantify the refraction coefficient. First, the  $C_r$  value in Eq. 3.5 was varied by iteration to match the calculated  $D_f$  value to the observed average maximum scour depth for each run CL1-CL9. The resulting values were plotted as a function of the calculated impingement angle  $\chi$  for each run. For an independent verification of this relation, the observed trajectory angle from the point of tailwater entry was determined for runs SH1-SH4. This method has the advantage of including scour over the full range of scour hole depth to equilibrium. The observed angle was determined by linear regression of the recorded horizontal coordinate ( $x$ ) of the maximum scour point as a function of the maximum hole depth ( $D$ ) over time for each fixed overfall run. Again the resulting values of  $C_r$  were plotted as a function of the calculated impingement angle for each run. Data from both methods of calculation are shown in Fig. 5.6, which shows the two methods to be consistent with each other. As predicted, the coefficient decreases as the impingement angle increases.

Linear regression of the refraction coefficients gives an empirical curve for determination of the jet trajectory angle:

$$C_r = 2.503 - 1.197\chi \quad (5.1)$$

where  $\chi$  is in radians. In theory, the value of  $C_r$  should drop to 1.0 as the impingement angle approaches 1.57 radians. The regression equation was used to calculate  $C_r$  for input to Eq. 3.5.

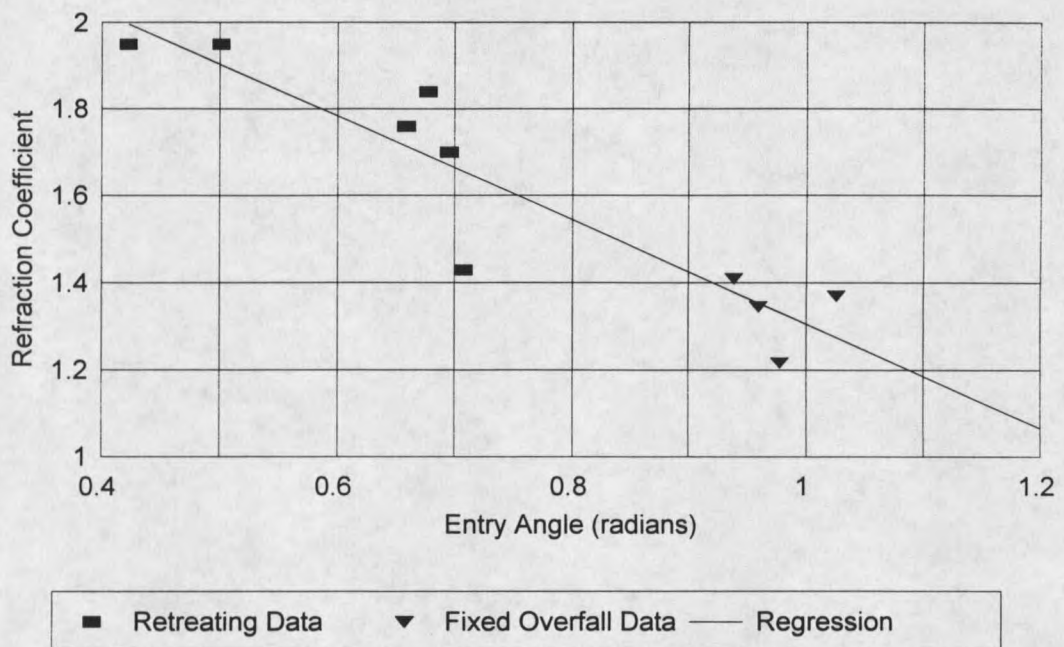


Figure 5.6. Regression of Trajectory Refraction Coefficient.

The assumption that the trajectory angle is constant, both at a given scour depth and over the full range of depths, is implicit in the empirical prediction function. From observation of the physical model, it is apparent that there is considerable fluctuation in the trajectory with time, and therefore that the angle might better be considered stochastically. However, a stochastic analysis was not attempted in this study. The angles used in developing the refraction coefficient were average values over the full range of hole depth

and over the range of longitudinal variation at a given scour depth in the layered soil case.

It is possible that experimental conditions in the flume influenced the observed trajectories for both clay and sand runs, due to nonaeration of the nappe. Because the overfall was sealed laterally by the flume walls, it is conceivable that pressure differences across the falling jet affected tailwater entry angles.

### 5.2.5 Final Scour Depth

Determination of the refraction coefficient  $C_r$  allows calculation of the final scour depth  $D_f$  according to Eq. 3.5. (Assume for the moment that mass failure length  $b$  can also be predicted, as described in a following section.) Table 5.5 shows the accuracy of model predictions for the final scour depth in retreating headcut runs. Observed ( $D_f^*$  obs) and model ( $D_f^*$  mod) values are listed, as well as refraction coefficient values for fixed overfall and retreating headcut runs. Observed  $D_f$  values were determined by averaging depths measured at frequent intervals over the data collection reach for each run.

Table 5.5. Modeled and observed maximum scour depth.

Run	SH1	SH2	SH3	SH4	CL2	CL5	CL6	CL7	CL8	CL9
$\chi$ (rad)	0.978	1.026	0.939	0.959	0.678	0.659	0.502	0.423	0.708	0.695
$C_r$	1.22	1.37	1.41	1.35	1.84	1.76	1.95	1.95	1.43	1.70
$D_f^*$ obs	---	---	---	---	0.271	0.391	0.487	0.520	0.313	0.310
$D_f^*$ mod	---	---	---	---	0.358	0.338	0.569	0.546	0.268	0.347

### 5.2.6 Scour Hole Shape

As described in Chapter 3, three points on the scour hole longitudinal profile must be located to define the model geometry: the maximum scour point ( $D_f$ ), the initial scour depth point ( $D_i$ ), and the toe point of the upstream limb. Analysis of fixed overfall data was done to determine the relation between the toe point and maximum scour locations. The transient nature of scour in the retreating headcut runs made a similar analysis impractical. It can only be assumed that scour shapes are similar between the two geometries.

Given the two dimensional location of the toe point, determined by the surface layer mass failure location, the objective is to determine the relative position of the maximum scour depth point. Values of scour hole half-width ( $X_m$ ) were determined from photos as the difference in the longitudinal position of the toe point and the maximum scour depth  $D$  at any time. Half-width values were plotted as a function of hole depth  $D$  for the fixed overfall runs, both normalized to the equilibrium hole depth  $D_e$  as shown in Fig. 5.7. Hole width ( $X_m/D_e$ ) is a well defined linear function of hole depth ( $D/D_e$ ). Linear regression of the data gives a slope of  $D/X_m = 0.545$ , with a corresponding slope angle of  $\tan^{-1}(0.545) = 28.6$  degrees. The slope angle is very close to the submerged angle of repose, 30.3 degrees, which gives a slope of  $\tan(30.3) = 0.584$ . The latter approximation is used in deriving model Eq. 3.5 for maximum scour depth.

### 5.2.7 Calibration of Scour Hole Shape Coefficient

An expression to represent the shape of the deeper portion of the longitudinal scour hole profile was also introduced in Chapter 3. The purpose of the shape coefficient

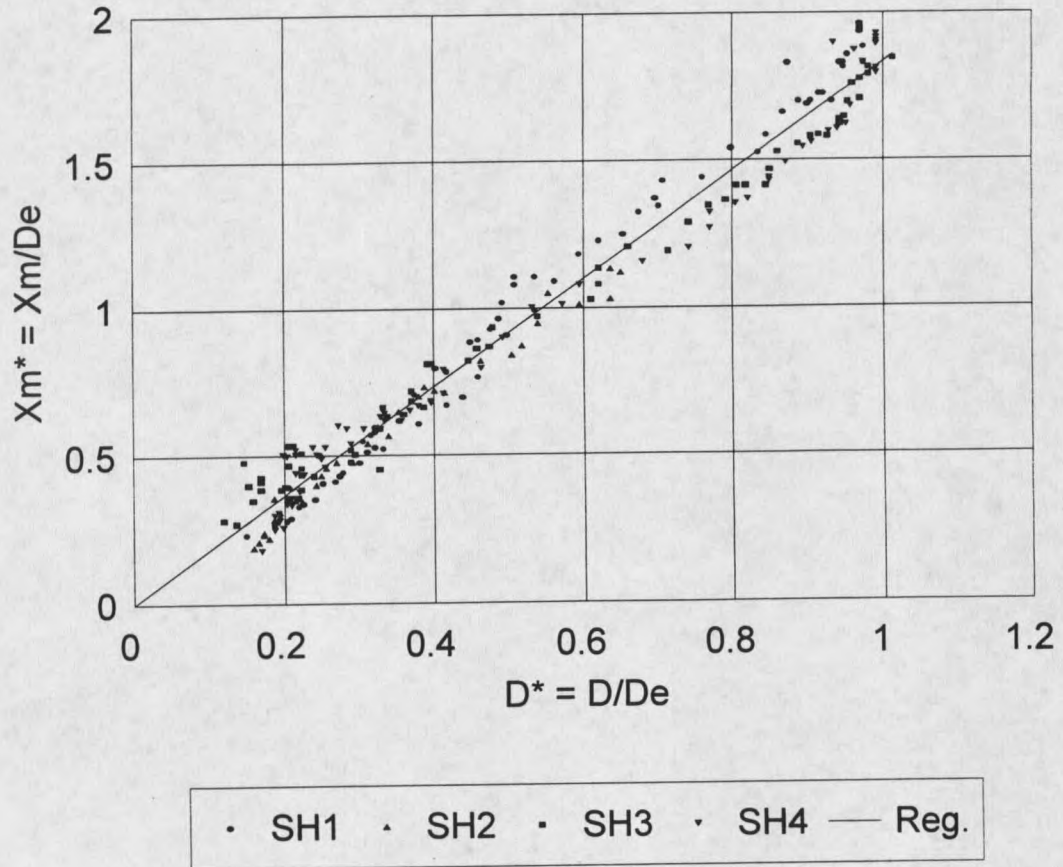


Figure 5.7. Scour Hole Width/Depth Relation.

proposed in Eq. 3.7 is to predict the initial scour depth  $D_i^*$  of the layered sediment failure cycle. Equation 3.7 presumes that the maximum scour depth  $D_f^*$  is known, as developed in preceding sections. Data from retreating headcut runs was used to quantify the dimensionless shape coefficient  $C_s$  for materials used in this study.

Equation 3.7 can be rearranged to represent differential scour ( $D_f^* - D_i^*$ ) as a linear function of mass failure length ( $b^*$ ):

$$D_f^* - D_i^* = C_s b^* \quad (5.2)$$

For experimental conditions, the value of the shape coefficient was determined by linear regression of differential scour as a function of dimensionless failure length for each data set. The  $D_f^*$  value used was the measured average maximum scour depth for each run. Due to the transient nature of the process, initial scour depth could not be directly measured during experiments. However, the duration of each failure cycle could be measured. This leaves  $D_i^*$  as the only unknown value in Eq. 3.1. Using Eq. 3.1, the “observed”  $D_i^*$  value for each data set was determined by iteration to match the model cycle period to the average observed period. The average observed mass failure length was used to calculate  $b^*$ . This procedure generates a single value of the shape coefficient for each data set CL1-CL9, according to Eq. 5.2. These values were then plotted as a function of  $b^*$  for each retreating headcut run, as shown in Fig. 5.8.

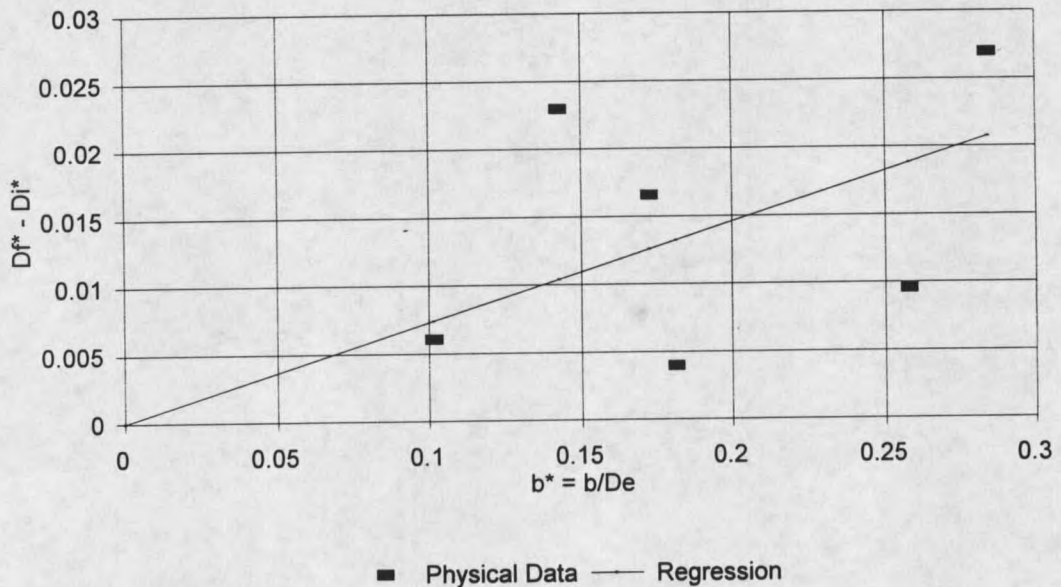


Figure 5.8. Regression of Scour Hole Shape Coefficient.

A linear regression line, constrained through the graph origin, was calculated for the data. The slope of this line, 0.073, is equal to the shape coefficient  $C_s$  and was used along with modeled values of  $b^*$  to calculate model values of  $D_i^*$  using Eq. 3.7. There is considerable scatter in the data, which can be attributed to several causes. As noted previously, the derivation assumes shape similarity over the range of scour hole depth and for different hydraulic conditions present in the various experiments. Other effects on the shape coefficient are further described below.

With model values for initial ( $D_i^*$ ) and final ( $D_f^*$ ) scour depths and mass failure length  $b^*$ , the failure cycle period can be predicted using Eq. 3.1. Initial scour depth must be equal to or greater than the jet potential core depth  $D_p$  to validate equation 3.1. For all retreating headcut runs,  $D_i^*$  was well in excess of  $D_p^*$ , suggesting that the equation can be used over a significant range of model variables. The accuracy of cycle period calculations are illustrated in Table 5.6, comparing observed ( $\Delta t_{obs}$ ) to modeled ( $\Delta t_{mod}$ ) cycle periods.

Table 5.6. Failure cycle period and initial scour depth.

Run	CL2	CL5	CL6	CL7	CL8	CL9
$\Delta t_{obs}$ (sec)	54	228	68	40	27	72
$\Delta t_{mod}$ (sec)	74	89	263	193	25	87
$D_i^*(obs)$	0.248	0.364	0.477	0.516	0.307	0.293
$D_i^*(mod)$	0.342	0.323	0.545	0.529	0.260	0.332
$D_p^*$	0.087	0.072	0.115	0.101	0.078	0.077

Observed periods varied by nearly an order of magnitude, from 27 to 228 seconds. Longer periods corresponded to thicker clay layers.

Several factors complicate the failure cycle period. Thick surface layers tend to collapse onto the upstream limb of the scour hole, forming a ramp for flow until the slab fully separates from the overfall. This armors a portion of the scour hole and causes a delay in the regular progression of downstream scour. The armoring effect is not directly accounted for in the mathematical model, although the resulting increase in cycle period is included in the physical data used for model calibration. The calculated initial scour depth is based on the measured period, and is therefore influenced by the armoring effect for some data sets. Armoring was noticed in particular during run CL5, which had the thickest clay layer. Adhesion of the clay to the flume walls tended to hold the failure slab in the ramped position beyond the time that slab separation would have otherwise occurred. For that reason, and only for run CL5, the failure mass was removed manually from the overfall after tension cracking indicated failure had occurred for each failure event.

Additionally, the position of the cohesive failure mass upon deposition in the scour hole has an effect. The failure mass remains primarily as an unbroken unit, and deflects flow around it. Depending on the mass position, it can protect the scour hole from further deepening or re-direct flow towards the upstream limb, causing accelerated scour there. Because failure slabs tend to impede downstream flow, there is also an influence on tailwater depth at the overfall. Thicker clay layers make both armoring and depositional position effects more dramatic. Thin layers fail very quickly and do not influence downstream scour to the degree that thick layers do.

For a given non-cohesive base soil, the proposed shape coefficient is a constant. If the scour hole shapes were similar for other non-cohesive materials, the same coefficient value would be valid. However, it is likely that there would be shape variations depending on soil properties. As described by Kobus et al. (1979), hydraulic parameters of the impinging jet also determine the scour form. It is apparent that scour in the layered model is more complex than at a fixed overfall. This makes it difficult to compare scour forms between fixed overfall cases and the current case where the impingement point migrates with headcut advance. The flow vector field for migrating scour is likely not the same as for fixed scour. Also, the Kobus et al. (1979) study examined only vertical jets, whereas the current study involves a range of impingement angles. Add to this the complicating factors introduced by mass failure, and the difficulty in case comparison becomes clear.

#### 5.2.8 Downstream Sediment Transport

In all experiments, the large majority of the mass failure material remained in the scour hole rather than becoming entrained and carried downstream. Clay slabs normally came to rest in the lower portion of the existing scour hole, becoming subsequently buried in redeposited sand. In many instances a characteristic deposition attitude was noted in that many slabs rested on edge in a nearly vertical position against the downstream scour hole limb. This tended to accentuate the obstruction of downstream flow. Only crumb or pebble size clay aggregates were entrained in downstream flow. In all cases the clay layer thickness was greater than normal flow depth.

Tailwater depth remained relatively constant over the run duration. This was

controlled by the flume discharge elevation, adjusted as desired by vertical positioning of the exit spillway. Immediately downstream of the active scour hole, sand and clay deposition caused the bed level to return to its approximate initial height with a constant slope to the discharge point. This indicates that the plunge pool erosion rate exceeded downstream flow transport capacity. Use of a discharge grade control point may have influenced the effect of downstream sediment aggregation. Kohl (1988) notes that "sediment deposition below headcuts often causes meandering which reduces the thalweg slope and increases the width." Of course the present flume conditions prevented any third dimension effects. With the exception of small channels, the redeposited soil surface was uniform both laterally and longitudinally. Some transient fluctuation of the tailwater depth occurred due to disruption of the normal flow pattern by clay slabs in the scour hole.

For model calculations, tailwater depth was input as observed for each run. No specific relation was used for prediction of tailwater depth. As presently formulated, tailwater level influences calculations through the cantilevered slab failure length, according to Eq. 3.16. Some method of predetermining tailwater level is necessary for a field application. A good approximation would be given by the normal downstream flow depth, measured from the initial downstream soil surface.

### 5.3 Cantilever Mass Failure

#### 5.3.1 Tensile Strength Measurement

Clay tensile strength as a function of moisture content was determined in a series of experiments independently from flume data collection. A simple cantilevered beam

model was used, as given in section 3.3.1. Values of flexural tensile strength were calculated based

Table 5.7. Retreating headcut mass failure parameters.

Run	$\omega$ (kg/kg)	Consolid. (Pa)	H (cm)	$b_{ave}$ (cm)	$\gamma_s$ (kg/m <sup>3</sup> )
1	.656	19495	3.28	8.73	1605
2	.634	22743	3.32	9.54	1618
3	.635	25992	3.09	9.03	1617
4	.596	35041	3.00	10.14	1642
5	.568	40000	1.53	9.74	1661
6	.565	45000	1.39	8.71	1663
7	.552	50000	1.37	9.68	1673
8	.572	65075	1.37	8.85	1658

on observed beam failure lengths. Eight total experiments were conducted, with parameters shown in Table 5.7. Failure lengths listed are the average of the several lengths measured for each experiment. Clay moisture content was varied from 0.552 to 0.656 by changing slab consolidation pressure. Initial moisture content prior to consolidation was 100% for all experiments.

From observation of the slab failures it was concluded that tensile strength was, as assumed, the controlling factor for beam stability. Prior to failure beam deflection was minimal, particularly for lower moisture contents. As the cantilever length was increased, tension cracks formed in a tightly spaced series across the beam width. After initial tension

crack appearance, the slab usually deflected slowly downward. At lower moisture contents, the tension cracks could be seen propagating downward to near the slab mid-point in some cases. At a certain deflection point the cantilever mass slumped suddenly into a fully failed position. It is likely that the slump coincided with compressive failure at the slab base. Based on this failure mechanism, it was reasoned that tensile failure occurs at the surface initially, determining the failure length, and that compressive stress prior to final failure is less than compressive strength. This is consistent with assumptions made in analytical development of the failure model.

Tensile strength was calculated for each failure event according to Eq. 3.10. An average of five data points were collected for each experiment at a constant moisture content. The neutral axis position was placed at the beam center for all calculations ( $r = 1.0$ ). Results graphed in Fig. 5.9 show tensile strength decreasing with increasing moisture content. Tensile strength values range from 10 kPa to nearly 50 kPa and are generally in agreement with the experimental results of Ajaz and Parry (1975). A direct comparison is not possible due to differences in moisture content range.

A power function was used to fit a curve to the data, shown as a solid line in Fig. 5.9. The curve was calculated according to the following equation:

$$\sigma_t (kPa) = 0.61 \omega^{-6.7} \quad (5.3)$$

Values of the constants were determined by data regression in log-log form. This equation is meant only to represent the limited data presented here. Equation 5.3 was used to calculate tensile strength values for analytical modeling of retreating headcut runs.















































